JGR Planets

RESEARCH ARTICLE
10.1029/2022JE007407

Key Points:

- We present a comprehensive map of structures in Tempe Terra which is available in GIS format
- Tempe Terra has experienced three distinct stages of tectonic activity which peaked in the Early Hesperian
- Tharsis-related extensional deformation did not begin in Tempe Terra until the Early Hesperian

Supporting Information:

Supporting Information may be found in the online version of this article.

Correspondence to:
C. J. Orlov,
eecjo@leeds.ac.uk

Citation:
Orlov, C. J., Bramham, E. K., Thomas, M., Byrne, P. K., Piazolo, S., & Mortimer, E. (2022). Structural architecture and deformation history of Tempe Terra, Mars. *Journal of Geophysical Research: Planets*, *127*, e2022JE007407. https://doi.org/10.1029/2022JE007407

Received 31 MAY 2022
Accepted 19 OCT 2022

Author Contributions:

Conceptualization: C. J. Orlov
Investigation: C. J. Orlov
Methodology: C. J. Orlov
Supervision: E. K. Bramham, M. Thomas, P. K. Byrne, S. Piazolo, E. Mortimer
Visualization: C. J. Orlov
Writing – original draft: C. J. Orlov
Writing – review & editing: C. J. Orlov, E. K. Bramham, M. Thomas, P. K. Byrne, S. Piazolo, E. Mortimer

Structural Architecture and Deformation History of Tempe Terra, Mars

C. J. Orlov[1], E. K. Bramham[1], M. Thomas[1], P. K. Byrne[2], S. Piazolo[1], and E. Mortimer[1]

[1]School of Earth and Environment, University of Leeds, Leeds, UK, [2]Department of Earth and Planetary Sciences, Washington University in St. Louis, St. Louis, MO, USA

Abstract The structurally complex region of Tempe Terra, located in the northeast of the Tharsis Rise on Mars, preserves deformation related to the growth of Tharsis and lies along the trendline formed by the Tharsis Montes volcanoes. We characterize the spatiotemporal tectonic evolution of Tempe Terra based on comprehensive structural mapping. From this mapping, we identified 16 cross-cutting fault sets and placed these in relative time order, based on a hybrid approach using cross-cutting relationships and buffered crater counting. We are thus able to provide a broad framework for understanding the timing of development for the Tharsis Rise and Tharsis Montes axial trend (TMAT). Our work shows that Tempe Terra has experienced three distinct stages of tectonic activity from the Middle Noachian to the Late Hesperian. Stage 1 involved E–W extension followed by localized NE–SW extension, which produced local zones of N and NW faulting through the center and west of Tempe Terra in the Noachian. Stage 2 produced intense NE-oriented faulting concentrated along the TMAT in the Early Hesperian as a result of a discrete period of NW–SE extension and local volcanism. Stage 3 involved NW–SE extension coinciding with Tharsis volcanic activity, which generated a regional fabric of ENE-trending graben distributed across Tempe Terra from the Early to Late Hesperian. We observe an overall peak in tectonic activity in the Early Hesperian and find that Tharsis-related extensional deformation in the form of NE-oriented radial faulting did not start in Tempe Terra until this time.

Plain Language Summary Despite decades of research into the Tharsis Rise, Mars's largest volcanic province, there is still uncertainty around the timing and mechanism of its development. Examining the deformation associated with Tharsis can help us understand these factors. Tempe Terra, an ancient plateau in the northeast of the Tharsis Rise, provides an excellent opportunity to do this because it preserves rocks and structures from Tharsis's early evolution and falls along a volcanic and structural trendline formed by the Tharsis Montes volcanoes. However, addressing the larger-scale evolution first requires understanding when and where structures in Tempe Terra evolved. We characterize the nature of these structures through time using comprehensive structural mapping. Our work shows that Tempe Terra experienced three distinct stages of tectonic activity across many hundreds of millions of years early in Martian history. We find that the majority of tectonic activity in Tempe Terra occurred in the Early Hesperian period (approximately 3.5 billion years ago). This time is also when we first see evidence in the area for the growth of Tharsis in the form of NE-oriented faults. We are thus able to provide a broad framework for understanding the timing of development for the Tharsis Rise and Tharsis Montes trendline.

1. Introduction

Tempe Terra is a structurally complex region situated at the northeast edge of the Tharsis Rise volcano-tectonic province (Figure 1). Crustal stresses associated with the development of the Tharsis Rise resulted in the formation of radial extensional features and concentric shortening features surrounding Tharsis (Figure 1) (Anderson et al., 2001). Despite decades of research into various aspects of the Tharsis Rise (e.g., Carr, 1974; Plescia & Saunders, 1982; Wilson & Head, 2002; Zhong, 2009), uncertainty remains around both the timing of the Rise's development (e.g., Anderson et al., 2001; Bouley et al., 2018; Phillips et al., 2001; Tanaka et al., 1991) and the mechanism of its growth (e.g., Banerdt et al., 1982; Mège & Masson, 1996; Solomon & Head, 1982; Tanaka et al., 1991; Wise et al., 1979)—both crucial knowledge gaps in our understanding of Mars's geological evolution.

Tempe Terra provides an excellent opportunity to investigate Tharsis-related deformation because it is one of the few large areas that preserves rocks and structures from the early evolution of Tharsis as it is not covered by younger lava flows (Figure 1). In addition, structures within Tempe Terra lie along the trendline formed by

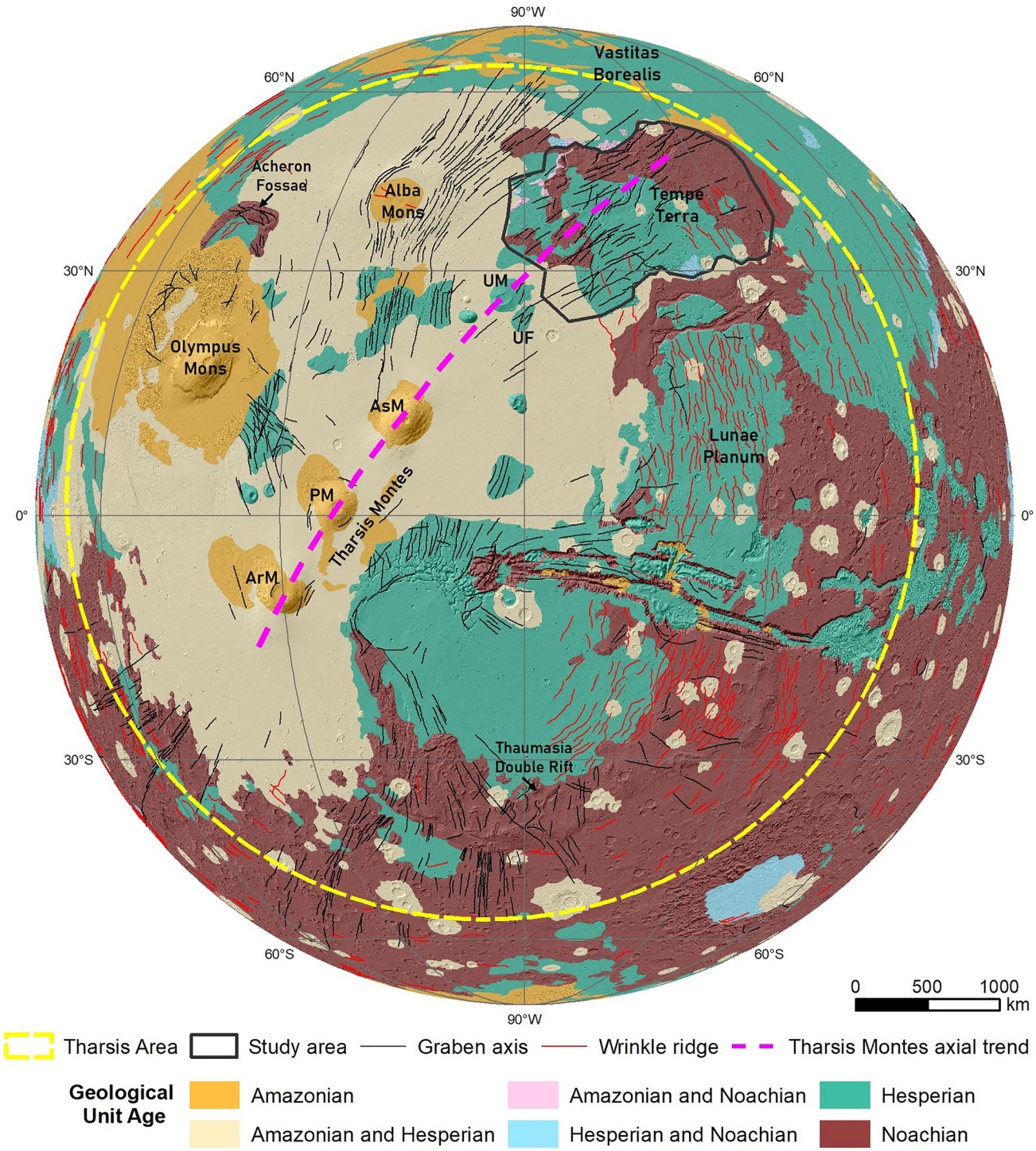

Figure 1. Geology map showing the regional context of Tempe Terra within the Tharsis Rise. Ages of simplified geological units from Tanaka et al. (2014) are draped over elevation from the High Resolution Stereo Camera-Mars Orbiter Laser Altimeter digital elevation model. Regional extensional and shortening structures from Tanaka et al. (2014) are included to demonstrate their radial and concentric patterns, respectively, relative to Tharsis. UM = Uranius Mons, UF = Uranius Fossae, AsM = Ascraeus Mons, PM = Pavonis Mons, ArM = Arsia Mons. Western hemisphere orthographic projection.

the alignment of the Tharsis Montes and Uranius Mons volcanoes, which we refer to as the Tharsis Montes axial trend (TMAT; Figure 1). This major volcanic and structural trend was identified in early Martian geological studies (Carr, 1974; Wise et al., 1979) but the timing of its development or its underlying mechanism has never been adequately explained, nor its relationship to Tempe Terra explored in any detail. Structures in Tempe

Terra therefore offer the opportunity to investigate several aspects of Tharsis's development—but before these large-scale evolutionary questions can be addressed, a detailed understanding of those structures in both space and time is required.

Here, we present the results of comprehensive structural mapping of Tempe Terra with the aim of determining the relative amounts of deformation through time. This detailed approach allowed us to capture the complexity of Tempe Terra's structural architecture and examine its history of deformation, primarily through the sequence of formation of fault populations. We separated mapped faults into sets and place them in relative time order based on their orientation, age, and cross-cutting relationships, and then calculated absolute model ages for each set to produce a timeline of Tempe Terra's structural evolution. We also generated regional fault maps to aid qualitative analysis of the structural architecture and spatial trends in tectonic activity through time. The resulting comprehensive inventory of structures is available in GIS format (Orlov, 2022). This work focuses on the location and timing of tectonic structures in Tempe Terra but lays important groundwork for further study of Tharsis. The unprecedented detail of our fault mapping allows us to provide initial constraints on the timing of development for the Tharsis Rise and TMAT, which can be combined in future with other datasets to more fully assess various evolution models proposed for Tharsis (e.g., Banerdt et al., 1982; Mège & Masson, 1996; Solomon & Head, 1982; Tanaka et al., 1991; Wise et al., 1979).

1.1. Geological Background: Tempe Terra

Tempe Terra is a ∼2 million km^2 plateau consisting largely of Noachian to Hesperian volcanic and highland units (Tanaka et al., 2014). It is bordered to the north by fretted terrain toward Vastitas Borealis, to the east by the lowland plains of Acidalia Planitia, to the south by the massive Kasei Valles outflow channel (which separates it from Lunae Planum), and to the west by a series of irregular Noachian basement blocks embayed by younger volcanic units (Figures 1 and 2). Tempe Terra is characterized by a widely distributed system of cross-cutting normal faults and graben that predominantly trend NE (Scott & Dohm, 1990). These extensional features contrast a region of shortening structures (wrinkle ridges) in the south (Watters & Maxwell, 1983).

On the basis of Viking image data, these extensional structures were grouped into two primary populations, and referred to as Mareotis Fossae and Tempe Fossae (Figure 2) (Carr, 1974). Mareotis Fossae consists of a set of long, subparallel graben trending NE to ENE that cover the north of Tempe Terra and have been associated with sub-surface dykes (Hauber & Kronberg, 2001; Mège & Masson, 1996). These structures have often been cited as some of the earliest evidence of Tharsis-related deformation (e.g., Anderson et al., 2001; Bouley et al., 2018; Scott & Dohm, 1990). Tempe Fossae is a more spatially extensive set of complex faults and graben trending NNE to NE (Figure 2), with some locally curvilinear fault trends and a series of deeper and broader graben (Hauber & Kronberg, 2001; Moore, 2001). Within the Tempe Fossae system is the Tempe Rift (Figure 2), which is a unique feature of the region interpreted as a rift by Hauber and Kronberg (2001) and has been the focus of previous structural studies of Tempe Terra (Fernández & Anguita, 2007; Hauber et al., 2010). The Tempe Rift is 1,400 km long and widens to the southwest along the rift axis (oriented N45–50°E) from a single deep graben to more distributed faulting with a complex set of several shallower, sinuous graben and half-graben (Fernández & Anguita, 2007; Hauber & Kronberg, 2001). The Labeatis Mons volcano and a second, older, unnamed volcanic center (which we label as "UV2" in Figure 2) are located within the rift structure and are considered to have been active syn- to post-rift, and pre- to syn-rift, respectively (Hauber & Kronberg, 2001).

The only previous assessment of regional fault sets and their timing within Tempe Terra was done by Scott and Dohm (1990). This work, and other studies of the structures in Tempe Terra (e.g., Fernández & Anguita, 2007; Golombek et al., 1996; Hauber & Kronberg, 2001; Moore, 2001; Wilkins et al., 2002), utilized Viking Orbiter imagery (resolution ∼200 m/pixel) and the geological map of Scott and Tanaka (1986). However, there has subsequently been some substantial revisions to the assignment of geological units across Tempe Terra in the new map by Tanaka et al. (2014). In light of these revised geological unit ages and the improved coverage of high-resolution imagery available since the mid-2000s, there is an opportunity to review the structural history of Tempe Terra in unprecedented detail.

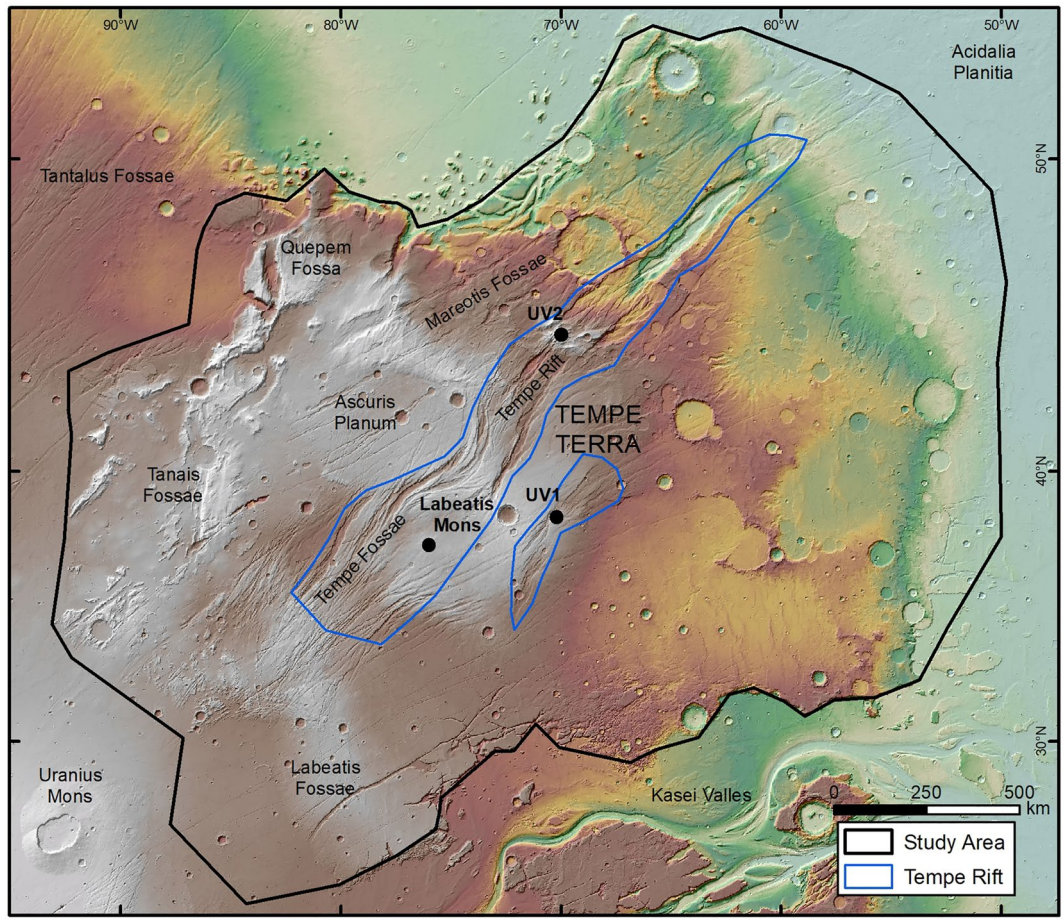

Figure 2. Shaded relief map of Tempe Terra showing study area, with elevation from colorized High Resolution Stereo Camera-Mars Orbiter Laser Altimeter digital elevation model. Major named features of Tempe Terra and surrounding area are labeled. The black dots indicate locations of main volcanic centers, UV1 and UV2 = unnamed volcanic centers. Mercator projection.

2. Data and Methods

This study is based on the analysis of high-resolution Mars satellite imagery to identify, map, and interpret structural features within Tempe Terra. We considered the entire Tempe Terra plateau in a 2.3 million km^2 study area (Figure 2) and primarily used images from the Mars Express High Resolution Stereo Camera (HRSC; Neukum et al., 2004; Jaumann et al., 2007), which have a typical resolution of 12.5–25 m/pixel. Daytime infrared image mosaics from the Mars Odyssey Thermal Emission Imaging System (THEMIS; Christensen et al., 2004), which have a 100 m/pixel resolution, were used to aid interpretation in areas of poor HRSC data quality.

2.1. Photogeologic Mapping

We used Esri ArcMap software to digitize all identified structural features at 1:300,000 scale, allowing for identification of faults down to ~1 km in size. Mapping was done in a Mars Mercator projection, preserving angular relationships. For simplicity, we mapped faults as independent polyline features based on observation of their surface appearance at the stated resolution. This means that hard-linked faults are mapped as single entities while soft-linked faults have been treated independently and mapped as separate entities. We make no assumptions about faults being physically connected in the subsurface, in order to avoid potential bias. Displacement on normal faults is visible in images as linear shadows or highlights created by variation in fault scarp height. Normal fault scarps were traced along their upper edge (i.e., where they cut the ground surface) as this was the most consistently visible boundary to map across faults. Where individual faults continued outside the study area

their full trace was mapped to avoid any truncation of fault length data. Wrinkle ridges were mapped as polylines along the approximate center of the ridgeline visible at the surface.

Geological photointerpretation can be affected by the angle of illumination in images, which can reduce contrast on features such as faults that are parallel to the illumination direction and potentially obscure them. To minimize this impact, whenever possible we used multiple images of a given area, acquired under a variety of illumination directions. Other limitations include the variation in the quality (e.g., signal-to-noise) of images and the extent to which the surface expressions of structural features are preserved because of post-tectonic modification (e.g., via mass wasting or ice-related processes). Consequently, scarps, canyons and other linear erosion features that may be structurally controlled have been excluded from the fault population. This conservative approach means we have likely undercounted structures in some areas, but our conclusions would not be meaningfully altered if so.

2.2. Fault Set Assignment

Once all faults were mapped, we separated the full population into a series of fault sets. Our working definition of a fault set consists of a group of faults that share a similar strike orientation and have consistent timing (i.e., stratigraphic relations) relative to other fault sets. Different fault sets do not necessarily indicate separate tectonic events. We used stratigraphic principles to determine relative ages of the faults. That is, that a fault must be younger than the geological unit (or units) it intersects, and cross-cutting relations between sets of faults, or between faults and other features, can be used to determine their relative order of formation and/or reactivation. Fault ages were initially determined from their intersection with the geological units of the 1:20,000,000 scale global map from Tanaka et al. (2014) (Figure 1). We also used the more detailed unit boundaries of the 1:1,000,000 scale map of the Tempe-Mareotis region by Moore (2001) to aid categorization of fault ages in the northwest of Tempe Terra. However, superposition relations with the geological units in both maps were not detailed enough on their own for unequivocally establishing relative timings given the complexity of faulting in the area. We therefore used an approach similar to Scott and Dohm (1990) where cross-cutting relations, fault morphology, and continuity of fault trends were also taken into account. Where we established that a fault system is continuous across a previously mapped geological boundary and that those faults have consistent morphology and trend, consistent with their having formed in a similar time and stress field, we grouped those structures together and assigned to them the youngest age of the units crossed. We then utilized available high-resolution images to examine cross-cutting relations between fault sets to establish their relative timing.

A major limitation of this stratigraphic approach to fault set age is that we can only assign a maximum age to faults in most cases. The youngest age we can assign from the Tanaka et al. (2014) geological units within Tempe Terra is "Amazonian and Hesperian" (Figure 1), and there are only a few places where units provide both upper and lower temporal bounds to fault formation. Other challenges include instances of unclear cross-cutting relationships, difficulty determining the relative order of non-intersecting sets of faults, and the possibility of fault reactivation—whereby later episodes of faulting might not have resolvably altered the appearance of a tectonic structure and so the relative age of that structure is overestimated.

2.3. Buffered Crater Counting

We used the buffered crater counting (BCC) method (Fassett & Head, 2008; Kneissl et al., 2015; Tanaka, 1982) to establish absolute model ages for fault activity in Tempe Terra through time, utilizing all mapped faults in the study area. These model ages are useful for refining the relative order of fault sets that have similar time-stratigraphic positions but do not otherwise interact, so would have an arbitrary relative position based on the stratigraphic approach alone. We also wanted to assess whether the fault sets in Tempe Terra are resolvably younger than the units they cross, something that is difficult or impossible to determine using only the distribution of geological units and their resolution in the current geological map of Tanaka et al. (2014). The BCC technique allows model ages to be determined directly for linear features such as faults, in contrast to the traditional crater counting method in which the age of a geological unit must be greater than the faults that cross it (essentially the same approach as in the use of stratigraphic relations) (Kneissl et al., 2015).

We used the catalog of Martian craters ≥1 km from Lagain et al. (2021), together with high-resolution Context Camera (CTX) images (Malin et al., 2007), to identify those craters that obscure or superpose faults, and thus formed after the last instance of fault activity in that locality. We followed the "ejecta approach" (Fassett &

Head, 2008; Kneissl et al., 2015), in which we included the ejecta blankets of craters (as well as the craters themselves) when determining superpositional relationships. Crater size–frequency distributions from BCC analysis were calculated with the CSFD Tools application (Riedel et al., 2018) for each fault set using a buffer factor of 2, correlating to a buffer width of twice the crater radius on each side of a fault. All faults within each set were included in the calculation of buffer areas whether they had postdating craters or not. This process was followed by a statistical analysis of the data with Craterstats 2.0 software (Michael & Neukum, 2010) to derive model ages using the two most commonly used chronology systems for Mars: the Neukum–Ivanov system (Hartmann & Neukum, 2001; Ivanov, 2001) and the Hartmann system (Hartmann, 2005). Martian epoch boundaries for both systems were taken from Michael (2013).

Statistical and systematic age uncertainties for BCC are the same as for other crater counting techniques (see Fassett, 2016; Michael and Neukum, 2010; Neukum et al., 2010; for a discussion of these uncertainties) but, as with cross-cutting relationships, the BCC method is also sensitive to fault reactivation (Kneissl et al., 2015). Since craters are instantaneous features whereas fault sets can grow over an extended period of time, craters that formed during ongoing fault activity may also be breached. Preserved craters included in the counting process therefore represent the end of formation or reactivation of a fault set (Kneissl et al., 2015). Given these inherent uncertainties and error ranges when determining absolute ages from BCC, we favored the relative age order established by cross-cutting relationships, and only relied on BCC ages where the relative order of sets is otherwise ambiguous. However, for the position of this relative order in absolute time, we utilized the BCC ages.

2.4. Fault Analysis

Fault length and orientation were determined for all digitized tectonic structures. To avoid distortions caused by our choice of map projection, all fault lengths were calculated as geodesic lengths and strike orientations as geodesic azimuths using the Tools for Graphics and Shapes plugin for ArcGIS (Jenness, 2011). For each fault set, we calculated statistics on lengths and orientations to further characterize set properties and provide a basis for set comparison. Strike orientations are presented as equal-area rose diagrams to avoid the distortions of a linear frequency scale (Nemec, 1988).

To quantify fault data patterns, we analyzed the spatial density of faulting using FracPaQ software (Healy et al., 2017) to create maps of estimated fault intensity for the total fault population and for specific time periods. Fault intensity is the total fault length in a given area, presented in units of m^{-1} (Dershowitz & Herda, 1992; Healy et al., 2017). The study area was covered by a grid of circular scan windows, and the number of faults intersecting the perimeter of each circle was used to estimate the fault intensity for the center of the circle (Healy et al., 2017). We set the diameter of our scan circles to ∼30 km, corresponding to half a degree of latitude on Mars, to capture regional-scale variations in intensity.

3. Mapping Observations and Regional Fault System Geometry

Normal faults that form graben are the main structural feature of the region (Figure 3a). Across Tempe Terra we mapped a total of 23,738 faults with a total cumulative length of 276,164 km, as well as 142 wrinkle ridges totaling 7,149 km (Figures 3a, Table 1). The regional architecture shows a concentration of structures through the center of the plateau in a ∼500 km-wide, NE-trending zone that follows the TMAT (Figures 2 and 3). This arrangement is reflected in the spatial distribution of fault intensity (Figure 3b), which also illustrates that the density of faulting within this zone, and across the plateau, increases to the west—that is, with greater proximity to Tharsis. The southeast quarter of the study area has the sparsest distribution of faults. This region is instead relatively well populated with wrinkle ridges (Figure 3a).

There are two primary trends in the fault population, one NE and one ENE (Figure 3a). These trends broadly correlate with the previously identified fault systems Tempe Fossae and Mareotis Fossae (Figure 2), respectively, and are radial to the Tharsis Rise. Despite the dominance of these NE-oriented trends, regions of N-oriented faulting and localized areas of NW-oriented faults are also present.

Individual faults are typically linear but with kinked traces characteristic of growth through linkage (Figures 4a and 4b) (e.g., McClay et al., 2002). However, curvilinear features are also found across Tempe Terra, particularly in the center of the study area where faults are strikingly curved or deflected around the Labeatis Mons volcanic

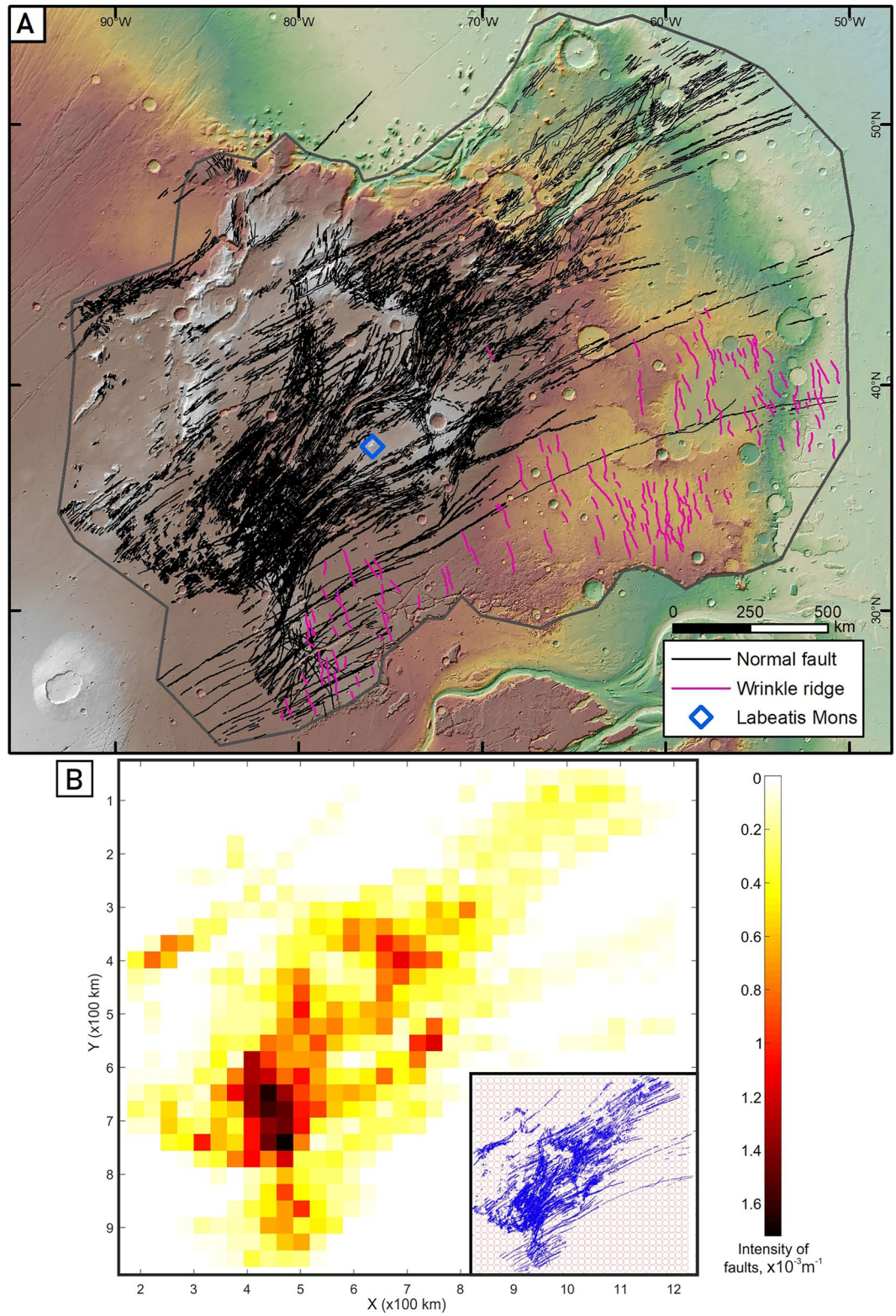

Figure 3. Structural features identified in mapping. (a) Map of Tempe Terra showing all normal faults and wrinkle ridges interpreted in this study. Mercator projection. (b) Estimated fault intensity map for total population of faults, highlighting a NE-trending zone of high intensity through the center. Inset shows grid of ~30 km diameter scan circles used to estimate intensity.

Table 1
Characteristics and Age of Tectonic Structures in Tempe Terra

Fault set	Trend	N_o	Strike (°)			Length (km)					Stratigraphic age			BCC–NI		BCC–H	
			Mean	Min	Max	Mean	Min	Max	L_{90}	ΣL	Epoch	Cross-cuts	Cross-cut by	Age (Ga)	Epoch	Age (Ga)	Epoch
All	NE	23,738	48	0	180	12	0.8	229	25	276,164	–	–	–	–	–	–	–
N1	N	70	7	350	22	16	2.2	49	27	1,112	MN		N2, H5, H6, H8, H11	3.9	MN	3.8	LN
N2	NW	82	306	273	338	11	1.9	48	19	894	MN	N1	H1, H5, H6, H8	–	–	–	–
N3	N	1,006	6	330	25	9	1.1	43	17	8,576	LN		N4, H5, H6, H8, H11	3.8	LN	3.6	LN
N4	NW	107	322	277	356	13	0.9	62	32	1,382	LN	N3	H5, H6, H8	3.8	LN	3.6	LN
H1	N	886	5	335	35	12	0.9	229	23	10,752	EH	N2	H2, H3, H5, H6, H7, H8, H9, H11	3.7	EH	3.6	LN
H2	NW	105	315	271	350	15	0.9	83	32	1,579	EH	H1	H5, H6, H8, H9	3.9	MN	3.7	LN
H3	NW	144	295	252	337	8	1.3	32	16	1,196	EH	H1	H11	3.7	EH	3.7	LN
H4	Circ.	755	64	3	178	9	1.3	65	18	6,725	EH		H5, H8	3.8	LN	3.6	LN
H5	NE	6,740	45	11	92	12	0.9	204	24	78,763	EH	N1, N2, N3, N4, H1, H4	H2, H8, H9, H10	3.7	EH	3.6	EH
H6	NNE	5,674	27	347	59	11	1	159	24	63,725	EH	N1, N2, N3, N4, H1, H5	H2, H3, H8, H9, H10, H11	3.7	EH	3.5	EH
HWR	NNW	142	344	316	8	50	10	179		7,149	EH	H1, H2, H5, H6	H7, H8, H9	–	–	–	–
H7	NE	388	52	27	82	16	1.2	198	35	6,068	EH	H1, H5	H8	3.8	LN	3.7	LN
H8	ENE	6,637	61	31	100	12	0.8	214	27	80,989	EH	N1, N2, N3, H1, H2, H4, H5, H6, H7		3.7	EH	3.5	EH
H9	ENE	333	58	43	73	15	1.2	110	32	5,052	AH	H1, H2, H5, H6		3.7	EH	3.5	EH
H10	ENE	141	57	36	77	19	1.2	103	38	2,704	LH	N3, N4, H5, H6		3.6	LH	3.4	EH
H11	ENE	659	55	14	102	10	0.8	118	22	6,572	AH	H1, H3, H6		3.6	LH	3.3	LH
A1	NNE	11	15	5	26	7	3	17	11	75	A			–	–	–	–

Note. Fault sets are listed in relative time order from oldest to youngest. N_o is the number of structures, ΣL is cumulative length, L_{90} is the 90th percentile of lengths (i.e., 90% of structures are ≤ this length). Stratigraphic epochs are from intersections with geological units of Tanaka et al. (2014). BCC–NI indicates buffered crater counting ages using the Neukum–Ivanov chronology system, and BCC–H indicates those using the Hartmann chronology system. MN = Middle Noachian, LN = Late Noachian, EH = Early Hesperian, LH = Late Hesperian, AH = Amazonian and Hesperian, A = Amazonian.

center (Figure 3a). Nearly all faults form pairs as part of a graben system (Figures 4b and 4c), and it is unusual to find isolated faults or step faulting outside of the Tempe Rift system. Most graben fit the "narrow graben" description of Mège et al. (2003), which have a high length-to-width ratio and consist of two parallel, segmented border faults. Many of the graben in the south tend to be even narrower, averaging just ~0.4 km wide compared with 1–2 km for graben across the rest of the area. En echelon graben geometry is common and individual graben may extend for tens or hundreds of kilometers along strike. The normal faults making up the graben are more segmented in detail than a lower resolution investigation would initially suggest, with many faults appearing continuous that in fact consist of numerous individual fault segments. These segments are typically arranged in en echelon patterns, and both soft linkage via relay ramps and hard linkage are common between segments (Figure 4a). This is reflected in fault length statistics, with individual segments only kilometers to a few tens of kilometers each despite the grabens they form typically being longer. Of the total regional population, the average fault length is 12 km (Table 1) and only 10% of faults are longer than 25 km (Table 1), reflecting the prevalence of shorter faults and the segmented nature of faults in the system (see Wilkins et al. (2002) for a discussion of the impacts of segment linkage on strain rate calculations in Tempe Terra).

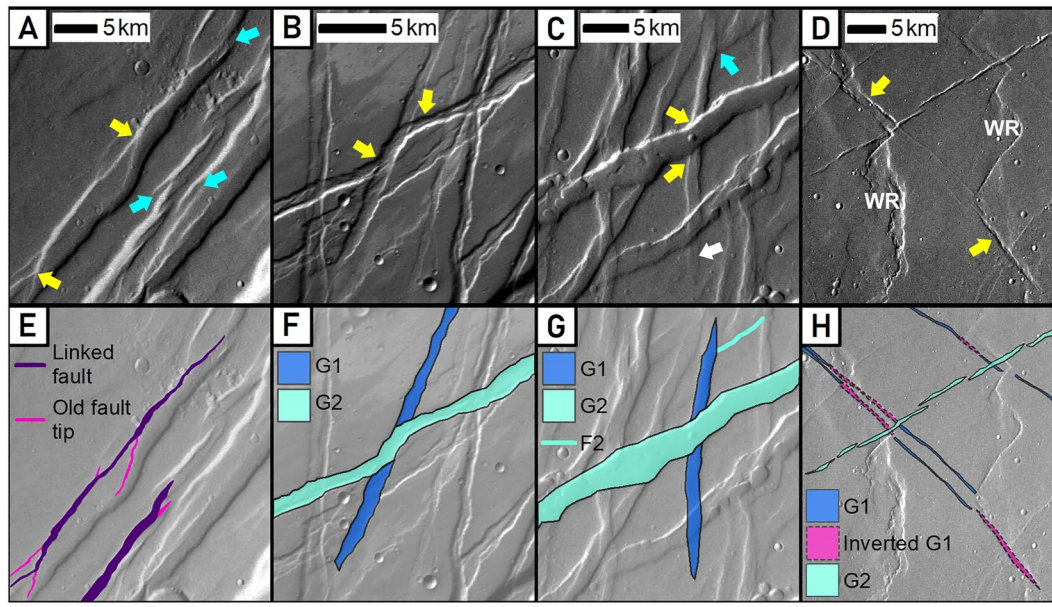

Figure 4. Fault characteristics and cross-cutting relationships. (a) Examples of fault linkage, with yellow arrows highlighting where faults are hard-linked and blue arrows indicating relay ramps where faults are soft-linked. (b) An example of a cross-cutting relationship producing a kinked path in a younger ENE graben as it interacts with an older NNE graben. Arrows highlight the offset fault trace of the younger graben. (c) An example of a cross-cutting relationship where older N graben are cut by a younger ENE graben. Yellow arrows highlight where the displacement of the older fault is interrupted and then continues on the other side of the younger graben. Blue arrow indicates a terminating fault relationship where a younger ENE fault tapers out against an older N fault. White arrow indicates where displacement tapers out toward fault tip. (d) An example of a cross-cutting relationship where younger N-trending wrinkle ridges (WR) invert segments of older NW graben. Inversion locations are marked by arrows. (e) Interpreted version of (a) showing trace of linked faults, as mapped, and abandoned fault tips from before linkage. (f) Interpreted version of (b) where G1 comes before G2. (g) Interpreted version of (c) where G1 comes before G2 and F2. (h) Interpreted version of (d) where G1 comes before wrinkle ridges, which then invert segments of G1, and wrinkle ridges and G1 are cut by G2. Images are from High Resolution Stereo Camera.

Cross-cutting relations between faults are typically expressed in the form of small offsets or kinks in the paths of younger faults where they cross pre-existing graben and partially link with the older faults before continuing their primary trend (Figure 4b). A series of such interactions can result in younger faults with zig-zag traces as they cross multiple pre-existing faults. In some cases, the relative timing of fault formation can be indicated by the vertical displacement visible in images. A normal fault will typically have the greatest displacement toward its center, and this will taper out to a minimum at each fault tip (Figure 4c) (Barnett et al., 1987). Where we observe a fault tip that tapers out against another fault, forming a terminating rather than cross-cutting relationship, we interpret this terminated fault as younger (Figure 4c). In other cases, faults that have their displacement interrupted, rather than tapering out, and then continue on the other side of a cross-cutting graben (Figure 4c), are interpreted as older. Younger faults can also be less well developed in regions where earlier phase faulting is intense, resulting in faults that are shorter, less numerous, less continuous, more isolated, and have less visible displacement.

Other structures that are common in Tempe Terra are pit crater chains and wrinkle ridges. Pit crater chains are linear features consisting of a string of pits and troughs, which are formed by collapse into subsurface cavities or explosive eruption (Wyrick et al., 2004). Pit crater chains are most common in the western half of Tempe Terra and typically follow existing graben trends. Wrinkle ridges are only found in the south of Tempe Terra, occurring across Early Hesperian and Middle Noachian units in areas with fewer extensional faults (Figure 3a). The ridges have sinuous forms and generally trend NNW. In the southwest corner of the plateau, some ridges have inverted sections of narrow graben, which create a zig-zig pattern along the ridge axes (Figure 4d). This reactivation of some pre-existing normal faults, combined with younger, cross-cutting normal faults (Figure 4d), allow us to place the timing of wrinkle ridge formation into context with fault activity, pointing to a narrow window for their development.

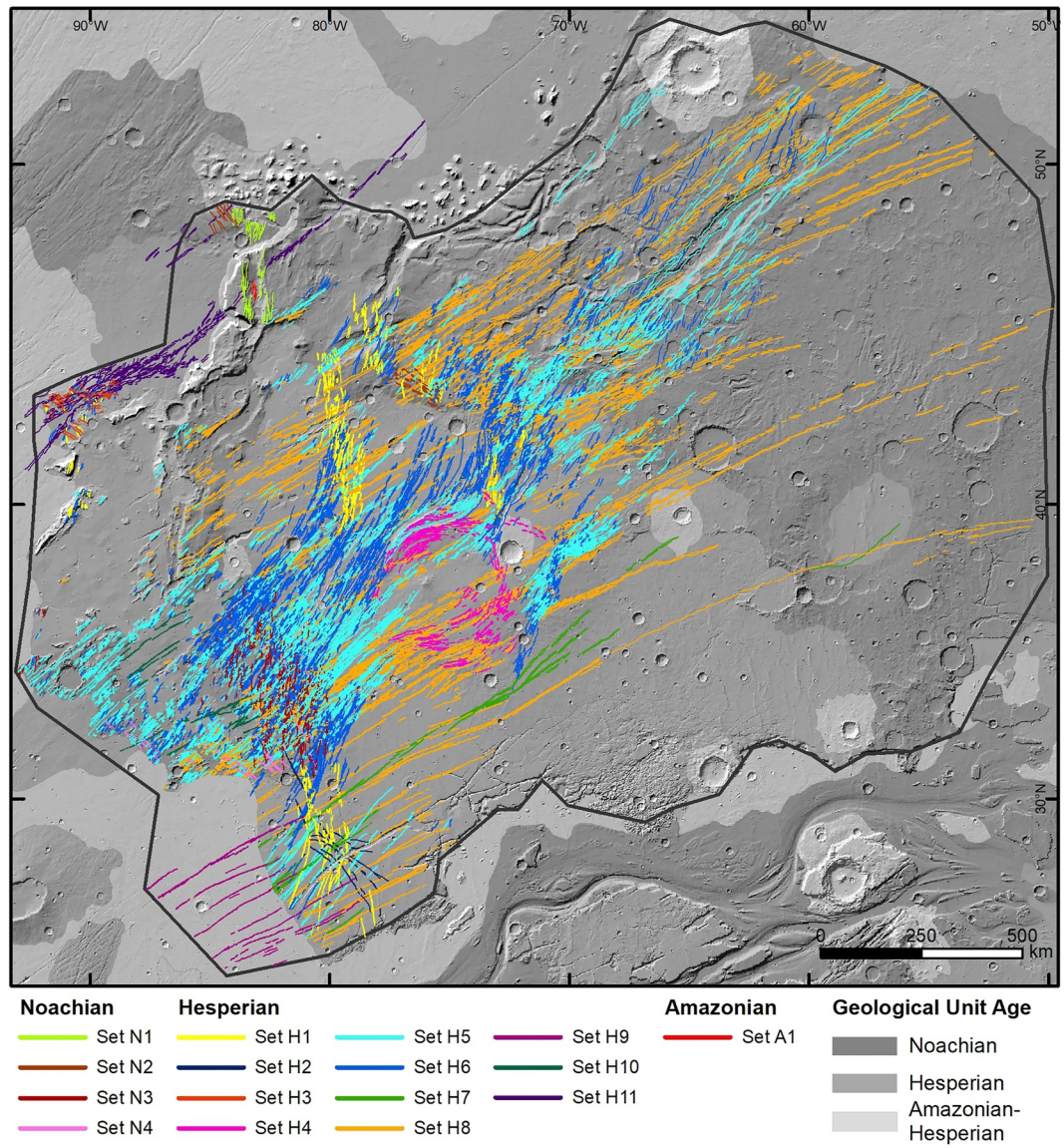

Figure 5. Map showing spatial distribution of all fault sets identified in Tempe Terra. Only normal faults from Figure 3a are included in sets. Individual fault sets are shown in Figures 7 and 8. Ages of simplified geological units from Tanaka et al. (2014) are draped over elevation from the High Resolution Stereo Camera-Mars Orbiter Laser Altimeter digital elevation model. Mars Mercator projection.

4. Fault Sets

We identified 16 fault sets consisting of numerous subparallel graben across Tempe Terra (Figure 5; Table 1). Set names are a combination of their specific period (e.g., "N" for Noachian) and a number signifying their order within that period based on cross-cutting relationships and/or BCC model results. Sets vary in scale from regionally extensive to locally confined and consist of tens to thousands of faults per set.

Stratigraphic ages range from Middle Noachian to Amazonian; we designate the majority of fault sets as Early Hesperian (Table 1). This is also the case for BCC-derived ages in the Neukum–Ivanov system, which is the system used in the Tanaka et al. (2014) map. In contrast, BCC ages based on the Hartmann system range from Late Noachian to Late Hesperian, and the most common fault set age is Late Noachian (Table 1). Between the two BCC chronology systems, the shape of the crater size–frequency distributions fit the Hartmann production function better in most cases (Figure 6). For a given fault set, ages between the two methods are generally consistent, especially considering error in the BCC ages—although in a few cases (sets H2, H4, and H7) the BCC

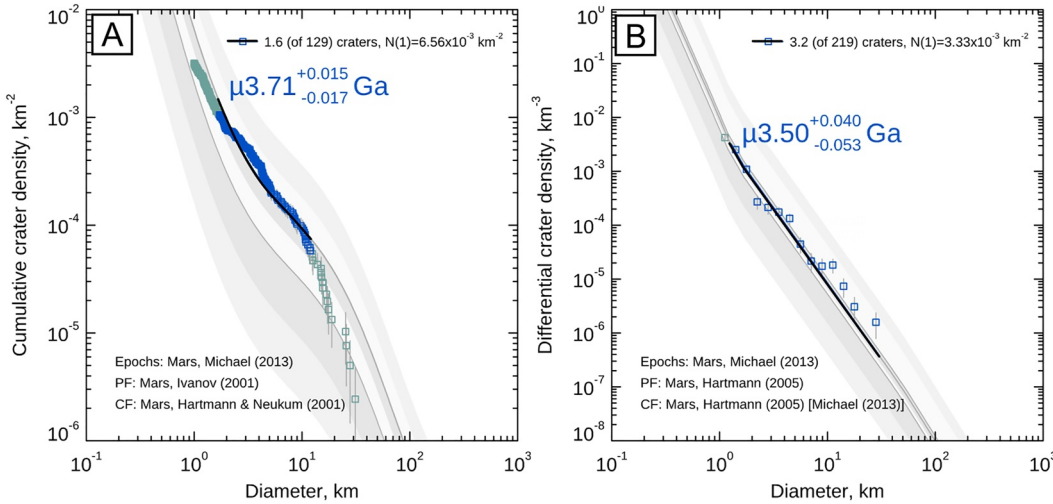

Figure 6. Crater count plots for set H5 comparing different age results. Errors shown are formal statistical errors regarding the isochron fit to the relevant portion of the plot. μ notation indicates these are model ages (Michael et al., 2016). (a) Cumulative crater-size frequency distribution using the Neukum–Ivanov chronology system showing an Early Hesperian age for H5. Data are unbinned. (b) Differential crater-size frequency distribution using the Hartmann chronology system also showing an Early Hesperian age for H5. Data are binned using the $\sqrt{2}$ method (Hartmann, 2005). PF = production function, CF = chronology function.

epoch assignments in both chronology systems contradict stratigraphic ages. The BCC model ages between the two chronology systems also vary, with Neukum–Ivanov ages being systematically older than Hartmann ages (Figure 6, Table 1). However, their correlating epoch is typically the same (i.e., a 3.8 Ga Neukum–Ivanov age and 3.6 Ga Hartmann age are both Late Noachian in their respective systems). These differences do not ultimately change our interpretation but are included here for completeness. Sets N2 and A1 did not have enough post-dating craters to enable BCC analysis. Isochron fits for all sets in both chronology systems are given in Figure S1 in Supporting Information S1.

4.1. Fault Set Geometry and Morphology

4.1.1. Middle Noachian Sets (N1 and N2)

The earliest preserved fault activity in Tempe Terra is Middle Noachian in age. Evidence of deformation is restricted to the north of the plateau and expressed as two localized fault sets which trend N and NW (Figure 7a). Set N1 consists of a large, N-oriented graben named Quepem Fossa (Figure 7a) that is ~30 km wide and 120 km long, as well as a cluster of small, linear graben along strike from this feature at the northern border of the plateau. Although eroded, Quepem Fossa preserves a series of faults along both sides of the graben structure. A prominent, N-trending feature potentially related to set N1 is Tanais Fossae ~300 km to the south (Figure 2). It consists of large, linear chasms that may have been structurally controlled, however, no clear faults are visible so this feature has not been included in the fault data set.

Set N2 consists of two small clusters of NW-oriented graben with a cumulative length less than 1,000 km (Table 1). Faults in the southern cluster fan outward slightly to the northwest, whereas those in the northern cluster are subparallel (Figure 7a). Overall, the structures comprising set N2 appear eroded, with younger infill on graben floors distorting cross-cutting relationships, although they do seem to cross-cut (and thus post-date) set N1.

4.1.2. Late Noachian Sets (N3 and N4)

Two fault sets are of Late Noachian age. They have similar N and NW trends to the Middle Noachian sets (Figure 7b). Faulting in this period is recorded in the west of the study area on highland blocks surrounded by Late Hesperian lava flows. Set N3 is the more extensive of the two sets and has a relatively high spatial density of N-oriented faults forming a swarm of narrow, subparallel graben (Figure 7b). Individual fault traces are

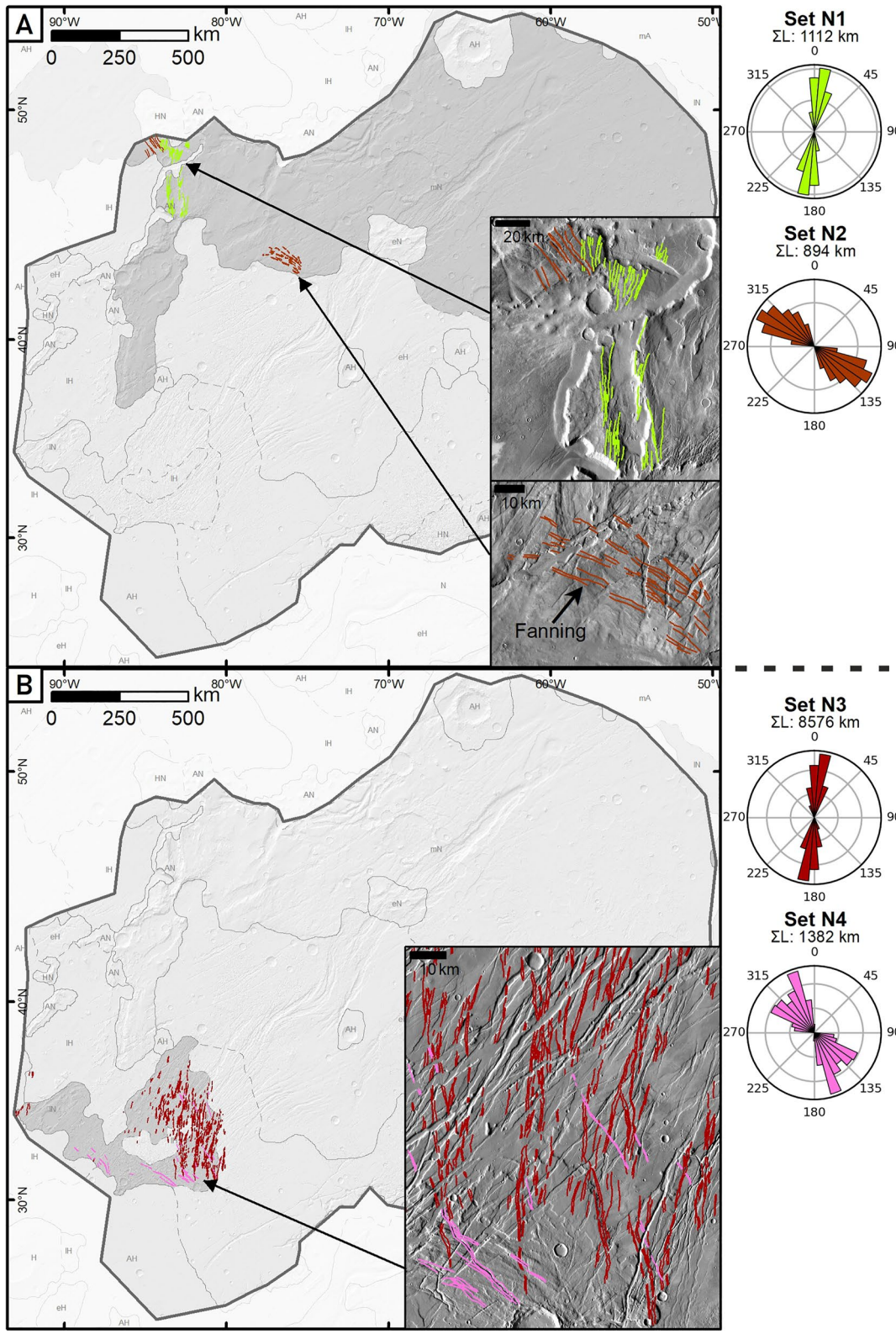

Figure 7. Noachian fault sets grouped by age. Base map is hillshaded High Resolution Stereo Camera-Mars Orbiter Laser Altimeter digital elevation model with thin, gray outlines indicating units from Tanaka et al. (2014). Rose diagrams of fault orientations are provided for each set. Σ*L* is cumulative fault length in kilometers. Insets show fault sets in detail with Thermal Emission Imaging System infrared daytime mosaic as base map. (a) Map of Middle Noachian fault sets N1 and N2 with Middle Noachian units shaded. (b) Map of Late Noachian fault sets N3 and N4 with Late Noachian units shaded.

comparatively short, averaging just 9 km, but this apparent shortness reflects at least in part their disruption by later Hesperian extensional structures, particularly H5 and H6 (Section 4.1.3). N3 also has a similar orientation to H1, which occurs to the north and south (Section 4.1.3). Set N4 consists of a small collection of NW-striking faults forming narrow graben with linear and curvilinear traces along the farthest western edge of the plateau (Figure 7b). N4 faults are longer on average than N3 but are more scattered and have more varied orientations.

4.1.3. Early Hesperian Sets (H1–H9)

We identified nine sets we interpret as Early Hesperian in Tempe Terra (Figures 8a–8c), pointing to a substantial increase in tectonic activity across the study area at that time. Along the western margin of Tempe Terra many of these sets are overlapped by Late Hesperian and Amazonian–Hesperian lava flows, providing an upper limit to the formation age of sets H3, H5, H6, H7, and H8. H1 is the first set from this period and continues the N trend of Late Noachian set N3. H1 forms several fault clusters spread across the study area (Figure 8a), including through the central horst block of the Tempe Rift. The faults form arrays of mostly linear graben, although there are also locally curvilinear features in the southwest of the plateau.

Set H2 is a small group of normal faults in the southwest of Tempe Terra forming very narrow, occasionally curvilinear graben with a variety of generally NW orientations. This set spans the large Labeatis Fossae flood canyon feature (Figure 2), and sections of some H2 graben have been inverted by wrinkle ridges (Figure 4d). Set H3 has similar orientation and timing to H2, but we separate these sets on the basis of the difference in morphology and considerable spatial separation without visible continuation of structures between H2 and H3. Set H3 consists of short, irregular, NW-oriented graben in a block of Early Hesperian terrain in the northwest of the study area (Figure 8a). Set H4 is distinctly different to any other set in Tempe Terra, and comprises a cluster of short, curvilinear faults and graben that are circumferential to the Labeatis Mons volcano and which form an almost complete ring (Figure 8a). Set H4 faults have a variety of orientations but those oriented NW to N are the least common, and faults on the western side of the volcano are missing or obscured by overprinting of extensive H5 and H6 faulting. To the southeast of Labeatis Mons, the interaction of locally NNE-trending H4 faults with ENE-trending H8 faults has created a series of rhomboidal fault blocks (Figure 8a, inset).

Sets H5 and H6 correspond to Tempe Fossae and together make up the Tempe Rift. Both sets form dense arrays of closely spaced, subparallel graben that are concentrated along the TMAT. Set H5 is an extensive set of NE-oriented faults that form a wide zone through the center of Tempe Terra (Figure 8b). Set H6 is equally extensive and also concentrated through the center of the study area, but with a dominant NNE strike (Figure 8b). The two sets do not have a definitive stratigraphic order as they often cross-cut each other, but incidences of structures of set H6 cross-cutting H5 are more common—and so we designate H6 as younger. Fault spatial density for both sets is highest in the region to the west of Labeatis Mons, where the structures of H5 and H6 interact with the N-oriented normal faults of N3, creating diamond-shaped horst blocks and some zig-zag fault traces, features first noted by Moore (2001). Sets H5 and H6 both form arrays of narrow, segmented, linear graben as well as larger rift graben that make up the Tempe Rift system. The Tempe Rift has a complex fault morphology, with right-stepping en echelon graben that are markedly wider (up to ∼20 km wide), and more curved than the typical graben we observe across the rest of the study area. In particular, the sigmoidal shape to the central portion of the rift where it curves around Labeatis Mons (Figure 8b, inset), and the visible localization of displacement onto a few large border faults (Figure 8b, inset), is not apparent to the same degree elsewhere in Tempe Terra. H5 is aligned with the rift axis, whereas H6 is oriented at a ∼20° angle to its main trend and makes up some of the oblique intra-rift faults described by previous authors (Fernández & Anguita, 2007; Hauber & Kronberg, 2001; Wilkins & Schultz, 2001). The fanning structure at 38°N, 70°W, which was regarded as being part of the Tempe Rift by Hauber and Kronberg (2001), is composed of a series of left-stepping en echelon graben and step faults from H5 and H6 in a zone parallel to the main rift and ending on the east side of Labeatis Mons. The fanning of these faults from either side of a central high (UV1 on Figure 2) creates its distinct "bow tie" shape (Figure 8b).

In the south of Tempe Terra, set H7 forms a long, linear graben system with a section of short, left-stepping en echelon graben (Figure 8c, inset). These faults are oriented NE to ENE, close to, but distinct from, the trend of set H8 which is rotated slightly clockwise relative to H7. The H7 structures on the eastern side fan outwards as they are seemingly deflected to the northeast around the Labeatis Mons center and the southern tip of the bow tie structure formed by sets H5 and H6 (Figure 8c). Graben from H7 and later fault sets cross-cut the population of wrinkle ridges discussed in Section 3. Set H8 consists of ENE-oriented faults that form a distributed array of long, linear graben that is largely continuous across the width of the study area (Figure 8c). This set includes

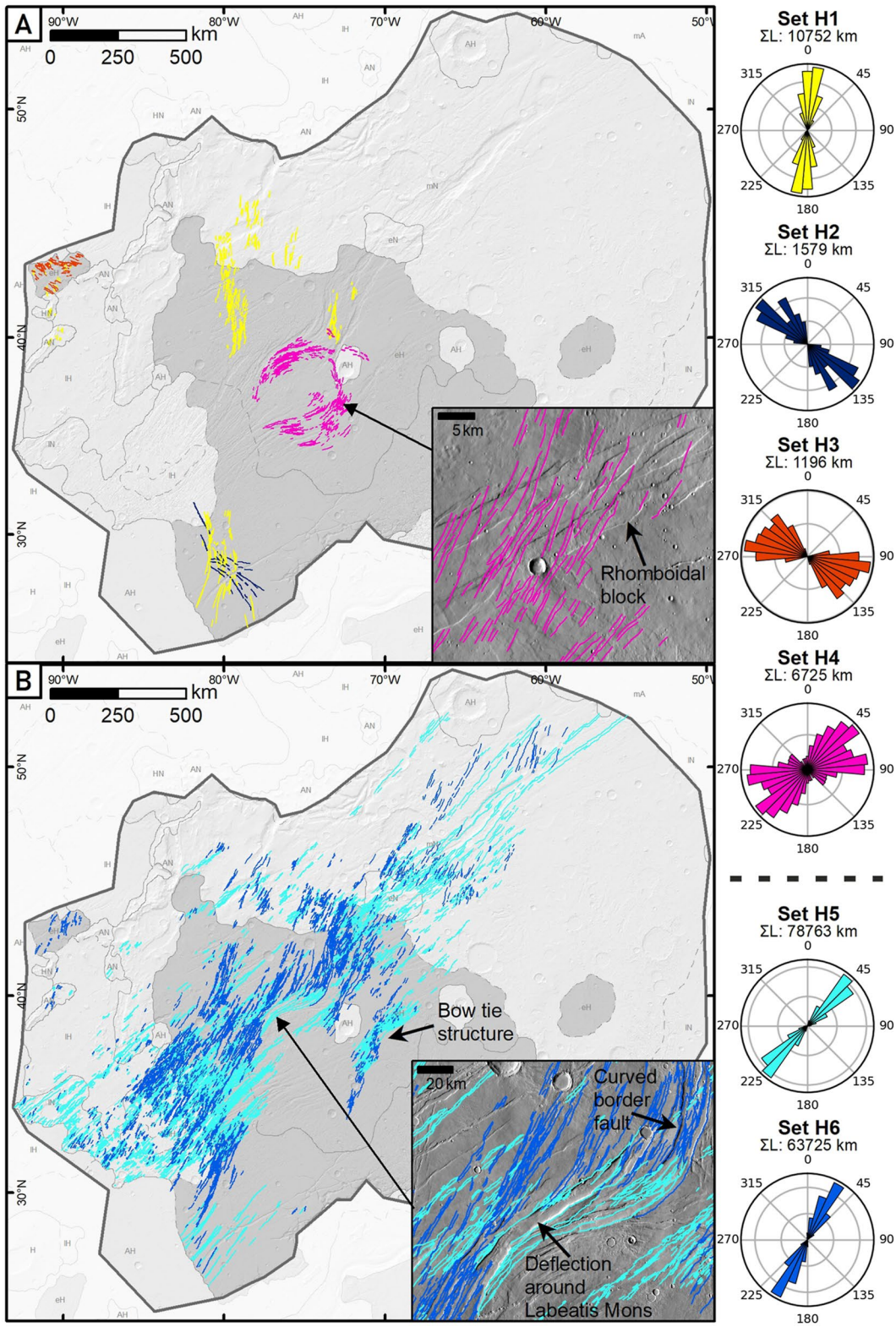

Figure 8. Hesperian fault sets grouped by age. Base map is hillshaded High Resolution Stereo Camera-Mars Orbiter Laser Altimeter digital elevation model with thin, gray outlines indicating units from Tanaka et al. (2014). Rose diagrams of fault orientations are provided for each set. Σ*L* is cumulative fault length in kilometers. Insets show fault sets in detail with THEMIS infrared daytime mosaic as base map. (a–c) Maps of Early Hesperian fault sets with Early Hesperian units shaded. (d) Map of Late Hesperian and Amazonian fault sets H10, H11, and A1 with Late Hesperian and Amazonian–Hesperian units shaded.

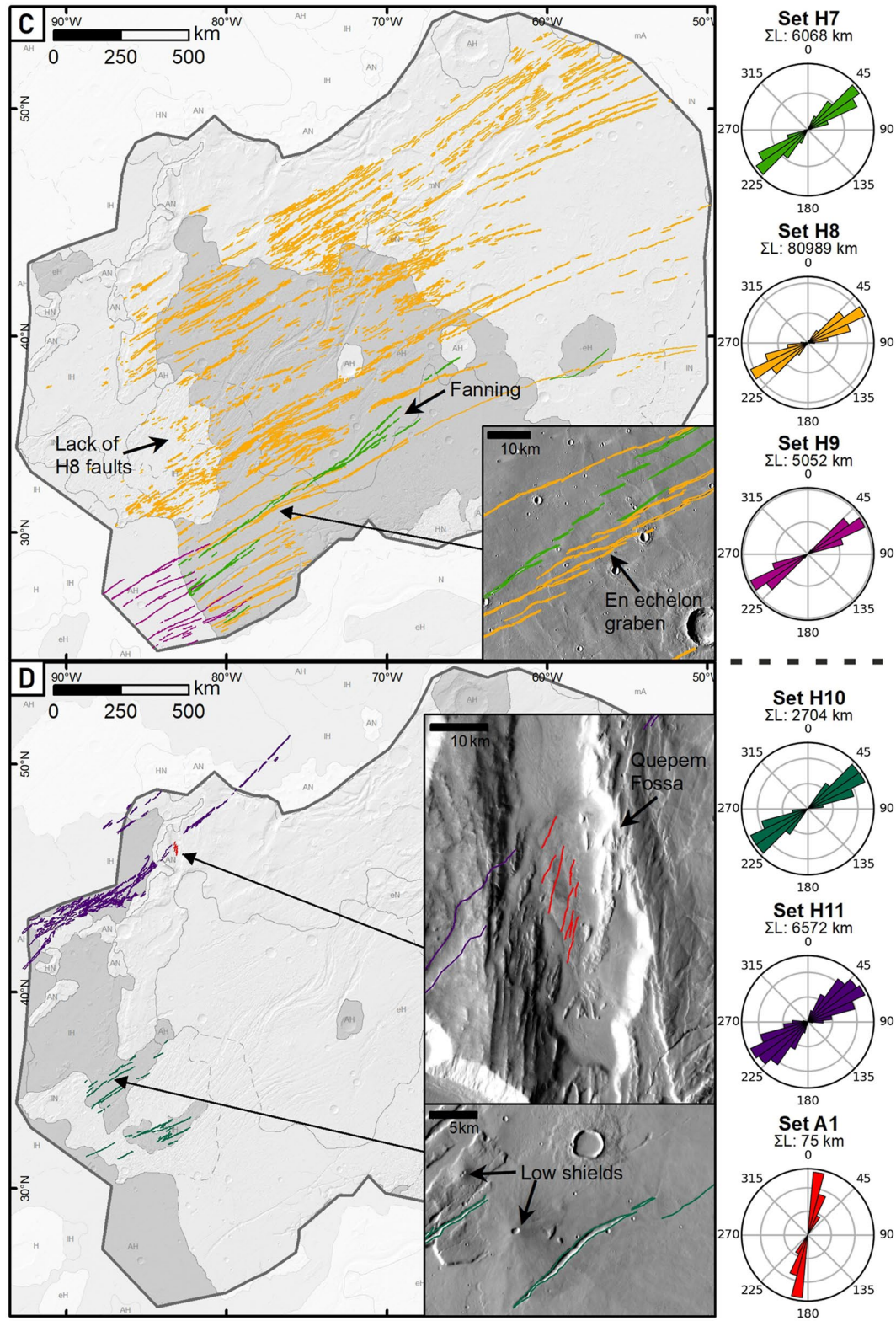

Figure 8. (Continued)

faults assigned to Mareotis Fossae. The H8 graben are more widely spaced than those within sets H5 or H6, and both left- and right-stepping en echelon graben geometry is present in several areas of the H8 set (e.g., Figure 8c, inset). Most H8 graben are linear and subparallel, except where they interact with curved faults of set H4 around Labeatis Mons, and in the northeast of the plateau where they fan slightly to the east. Fault traces are often slightly offset or zigzag in shape where they intersect with earlier extensional structures such as those in sets N3, H5, and H6 and, overall, H8 structures are fewer, shorter, and less continuous in areas where H5/H6 faulting is most intense (Figure 8c). Most pit crater chains are associated with this set or follow the same ENE trend, and Ascuris Planum has many linear chasms that also align with this orientation (Figure 2). At the southwestern margin of the study area, set H9 continues the trend of H8, with a widely spaced arrangement of narrow, linear graben orientated ENE (Figure 8c) that form right-stepping, en echelon graben segments. Unlike set H8, the extensional structures of set H9 cut through Amazonian–Hesperian volcanic units and continue onto the Early Hesperian units of the plateau. Graben of this set continue along strike outside the study area to the southwest toward Uranius Fossae and Ascraeus Mons (Figure 1). Despite similarity in the general orientation and overall timing of sets H7, H8, and H9, we have separated them as they form three distinct groups with cross-cutting relationships.

4.1.4. Late Hesperian Sets (H10 and H11)

We interpret two fault sets as Late Hesperian in age. This fault activity is concentrated along the western boundary of Tempe Terra, following a similar ENE trend as Early Hesperian sets H8 and H9 (Figure 8d). Set H10 consists of ENE-oriented, linear graben that cut through the smooth, Late Hesperian lava flows that embay the older, heavily faulted Noachian terrain in this area. Graben of this set are commonly associated with volcanic features such as vents and low shields (Figure 8d, inset) (Moore, 2001). Set H11 comprises ENE-oriented faults that cut through Amazonian–Hesperian and Late Hesperian lava flows and also continue across older plateau units at the northwest corner of Tempe Terra (Figure 8d). Although most of these normal faults form graben, some remain isolated, and in both cases there is a combination of linear and curvilinear traces. H11 features continue outside the study area to the northeast and southwest and connect with the Tantalus Fossae system from Alba Mons, which extends north from Ceraunius Fossae and then turns to the northeast (Figure 1) (Tanaka, 1990).

4.1.5. Amazonian Sets (A1)

The youngest faulting we have identified in Tempe Terra is Amazonian in age, based on faults cutting units interpreted by Butcher et al. (2017) as Amazonian glacial sediments. Set A1 is a small, localized group of short faults oriented NNE that do not form graben systems like the other sets. These faults are exposed on the floor of Quepem Fossa, the large N-oriented graben structure associated with set N1 in northwest Tempe Terra (Figure 8d, inset).

5. Discussion

5.1. Timing of Fault Activity

The ages we determined with the BCC method provide the fault sets with a useful anchor to the absolute model timescale of Mars. However, this process has significant statistical and systematic errors (Michael & Neukum, 2010; Neukum et al., 2010) that mean such model ages are best used in conjunction with observable superposition and cross-cutting relationships. These errors include our ability to accurately extrapolate the lunar chronology model to the cratering record on Mars, the choice of production and chronology functions and uncertainties within these functions, and the effects of small-number statistics in the case of there being relatively few impact craters proximal to a given fault set (Michael & Neukum, 2010; Neukum et al., 2010).

It is common within our results for multiple fault sets to have ages within the formal errors of each other, and therefore to be statistically indistinguishable. This outcome means—perhaps unsurprisingly—that the crater ages alone are not useful in many cases for discriminating relative age order between fault sets. BCC may also return an age that conflicts with the age of the faulted geological unit and observations of cross-cutting relationships. For example, set H7 has a Late Noachian age in both chronology systems using the BCC method, but sits within an area mapped by Tanaka et al. (2014) as Early Hesperian, and has cross-cutting relations that indicate its relative position between other Early Hesperian sets. In such cases, we have preferred the age implied by cross-cutting relations or, if the BCC-derived age is within error of the epoch boundary, we assigned the set its geological unit age (e.g., for set H1), resulting in some inevitable inconsistencies. However, it is worth bearing in mind that the stratigraphic units we are using come from a global geological map at 1:20 million scale where none of the crater

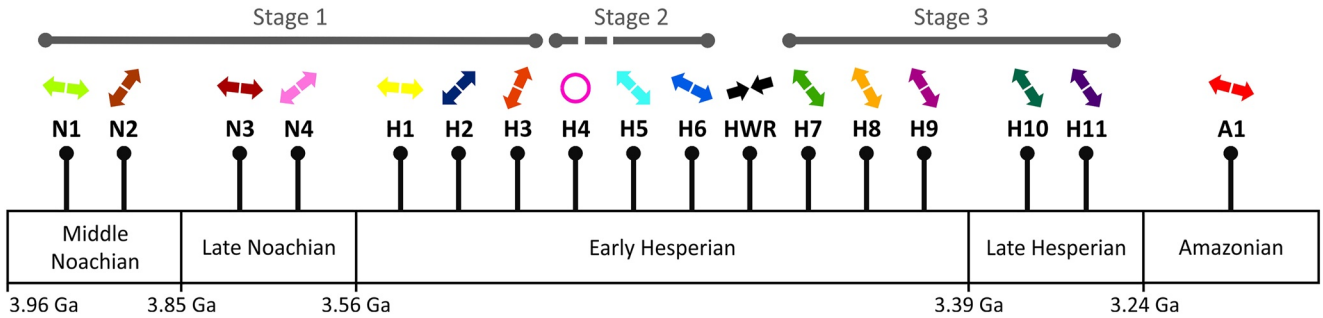

Figure 9. Timeline of Tempe Terra's deformation history, with three major stages of tectonic activity indicated. All fault sets are positioned in relative order and placed within their specific epoch. Epoch boundary ages are from Michael (2013) using the Hartman system (Hartmann, 2005). HWR = Hesperian wrinkle ridges. The arrows indicate a first approximation of extension direction based on the simplified assumption that σ3 is perpendicular to the average strike of each set. The circle indicates circumferential faulting around Labeatis Mons. Colors correlate to Figures 5, 7 and 8. Movie S1 in Supporting Information S1, shows an animated version of the timeline in conjunction with the fault map.

counting type localities for the different units are within Tempe Terra (Tanaka et al., 2014). The current global geology map therefore does not have the fidelity and resolution we would ideally like to match the detail of our fault mapping in Tempe Terra. Issues arising from small-number statistics also likely play a role, given that the nature of BCC analysis means we have a very limited number of craters to draw statistics from, especially for smaller fault sets, and because statistical error depends on the number of craters counted (Neukum et al., 2010).

Nonetheless, despite these limitations, we were able to search for anomalously young faulting in Tempe Terra and found that this was not the case, given that most fault sets have Late Noachian or Early Hesperian ages based on the BCC method. We were also able to use BCC results to provide additional constraints on fault set age and relative order, either where we had little option but to assign relative stratigraphic positions arbitrarily due to a lack of cross-cutting relations, or when a geological unit age is given as a range, such as the Amazonian and Hesperian Volcanic Unit (AHv) (Tanaka et al., 2014). For example, with this approach we were able to assign sets H9 and H11 from within the AHv unit as Early Hesperian and Late Hesperian, respectively. Ultimately, the combination of stratigraphic and BCC-based approaches has been beneficial in refining the relative positions of fault sets in sequence and determining the absolute timing of tectonic activity in Tempe Terra. For future refinements of Tempe Terra's structural history, a more detailed geological map that utilizes local crater statistics covering all of Tempe Terra would be extremely valuable in further improving interpretation of tectonostratigraphic relationships.

5.2. Stages of Deformation in Tempe Terra

Tempe Terra has experienced multiple episodes of tectonic deformation, resulting in a complex pattern of cross-cutting normal faults and wrinkle ridges. Although from our mapping we have identified 16 faults sets, not all of these sets necessarily reflect separate episodes of extension or distinct stress fields. Instead, the fault activity in Tempe Terra can be broken up into three primary stages based on timing and principal orientations (Figure 9):

Stage 1) N- and NW-oriented faulting through the center and west of the study area from the Middle Noachian to the beginning of the Early Hesperian;
Stage 2) intense NE-striking faulting concentrated along the TMAT during the Early Hesperian; and
Stage 3) ENE-oriented faulting distributed across Tempe Terra during the Early and Late Hesperian.

Stages 1 and 2 are separated by a major shift in the orientation of the extensional stress field, whereas Stages 2 and 3 are separated by a period of crustal shortening and the development of wrinkle ridges (HWR in Figure 9).

Stage 1 is characterized by several sets of N- and NW-oriented extensional structures (Figure 9), with activity focused in patches across the center and west of Tempe Terra (Figure 10a). The N-striking fault sets—N1, N3, and H1—are the dominant features of Stage 1, forming spatially dense regions of graben across larger areas, whereas the NW-striking sets—N2, N4, H2, and H3—form as smaller, localized zones of deformation. This dominance of N- and NW-oriented faulting prior to the onset of Early Hesperian-aged, Tharsis-radial faulting indicates a different stress regime was active in Tempe Terra compared to other early phases of tectonic activity

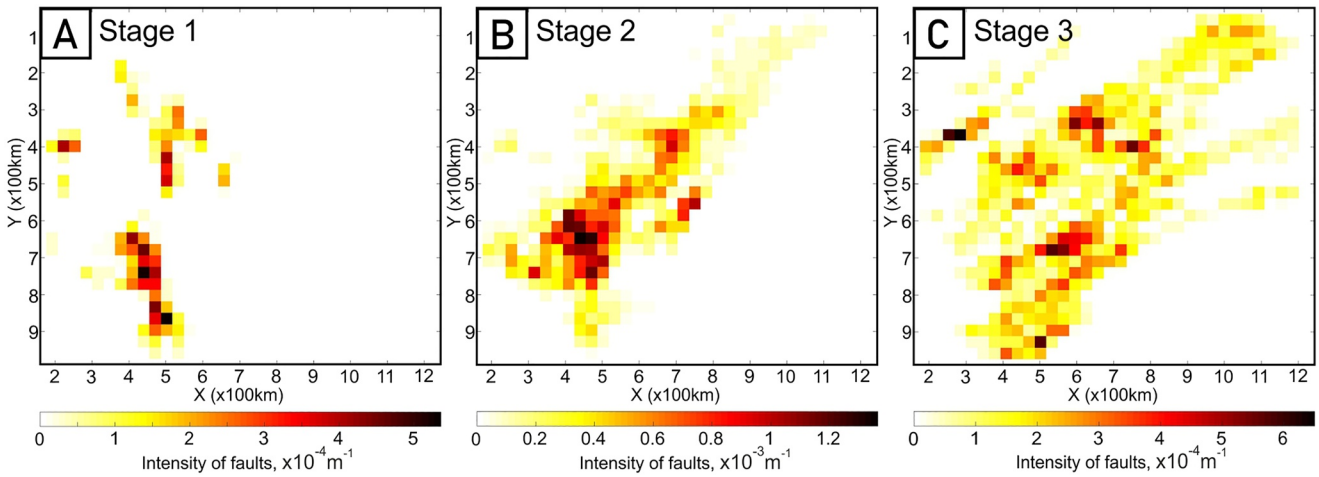

Figure 10. Estimated fault intensity maps for each stage of deformation. (a) Estimated fault intensity for Stage 1 fault sets (N1, N2, N3, N4, H1, H2, H3). (b) Estimated fault intensity for Stage 2 fault sets (H4, H5, H6). (c) Estimated fault intensity for Stage 3 fault sets (H7, H8, H9, H10, H11).

in the south of Tharsis. Other major, non-radial structural systems around Tharsis include Acheron Fossae and the Thaumasia Double Rift (Figure 1) (Hauber et al., 2010).

The current grouping of sets within Stage 1 shows three episodes of N-striking normal faulting followed by NW-striking normal faulting (Figure 9). This repeating pattern may be real or may simply be an artifact of the uncertainty in age assignments—and thus instead could represent a single period of N-oriented faulting followed by NW-oriented deformation. N-oriented sets N3 and H1, which have the greatest number of faults and total cumulative length of all Stage 1 sets (Table 1), share a strong continuity in orientation, location, and timing. Therefore, despite being separated based on the units they cross-cut, these two sets likely developed as part of a continuation of the same deformation event. Stage 1 fault sets are more local in scale compared with those from later stages, and account for just 9% of cumulative fault length in Tempe Terra. However, it is likely more faults from this phase would be visible if not covered by later Hesperian lava flows. This potential lack of structure preservation makes it difficult to assess the true scale and intensity of Stage 1 activity. In terms of model ages for Stage 1 faulting, the sets are all Late Noachian in the Hartman system, ranging from 3.8 to 3.6 Ga, and Middle Noachian to Early Hesperian in the Neukum–Ivanov system, from 3.9 to 3.7 Ga (Table 1). These results indicate that Stage 1 activity lasted (per our models for Martian impact cratering) for ~200 Myr and thus represents either a single period of E–W-oriented crustal extension followed by localized NE–SW-oriented extension, or a repeating cycle of both E–W- and NE–SW-oriented extension in the Noachian. Stage 1 ended with the onset of volcanism at Labeatis Mons and the transition to the predominant NE-striking volcano-tectonic trend.

Stage 2 consists of faults from the circumferential H4 set and the NE-oriented sets H5 and H6 (Figure 9), which together create a localized zone of high fault intensity (Figure 10b) concentrated along the TMAT (Figure 1). The transition from Stage 1 to Stage 2 is marked by the development of a strong spatial and temporal relationship between tectonic and volcanic features. Stage 2 includes the development of the Tempe Rift, which is deflected around Labeatis Mons and interacts with the local fault set H4, which is associated with the volcano. Faulting from this stage is extensive, accounting for 54% of total cumulative fault length, but this deformation is not evenly distributed across Tempe Terra (Figure 10b).

Sets H5 and H6 are potentially coeval, as their mutual cross-cutting relations are not fully consistent. Further, under an oblique extensional regime, which has been interpreted for the Tempe Rift by Fernández and Anguita (2007) and is discussed in more detail in the next section, two coeval fault sets with different trends can be generated in the same faulting episode (Henza et al., 2011; Schlische et al., 2002). The BCC-derived ages of sets H5 and H6 are also within formal statistical error of each other, meaning we cannot separate them based on this model age approach. In both chronology systems, Stage 2 fault activity began in the Late Noachian but mostly occurred at the start of the Early Hesperian (Table 1), lasting less than ~100 Myr. Stage 2 represents a single, major deformation event over a relatively short period of time in the Early Hesperian, marked by local volcanism and NW–SE extension focused along the TMAT. This stage ended with a shift to ENE–WSW compression and the

formation of wrinkle ridges in the south of the plateau. Clear cross-cutting relations with faults of Stage 1 and Stage 3 (Figure 4d) place wrinkle ridge development close in time to Stage 2 faulting. The apparent dearth of wrinkle ridges in the areas of most intense normal faulting (Figure 3a) suggests that the primary phase of crustal shortening in Tempe Terra either came after the majority of Stage 2-related extensional faulting or was active concurrently but ridges did not develop where extension dominated further north. Our finding of Early Hesperian shortening is consistent with existing models for the timing of the Tharsis-wide development of wrinkle ridges (Anderson et al., 2001; Bouley et al., 2018; Tanaka et al., 1991).

During Stage 3, a pervasive regional fabric of distributed graben that trend ~ENE across most of Tempe Terra developed (Figure 10c), broadly radial to Tharsis. Activity from this stage is reflected in sets H7, H8, H9, H10, and H11, all of which have similar orientations (Figure 9). This activity also includes faults attributed to Mareotis Fossae (Figure 2). These sets account for 37% of cumulative fault length in Tempe Terra, but Stage 3 faults appear shorter and less numerous in areas where Stage 2 faulting is most intense (Figures 8c and 10c). This observation could be accounted for by faults from the earlier episodes of extension acting as lateral barriers for later stages of faulting, limiting their along-strike propagation and growth (Henza et al., 2011). This effect is only evident where earlier fault sets from Stage 1 and 2 are well-developed, such as at the western end of the TMAT (Figure 8c), in agreement with the model observations of Henza et al. (2011).

Later fault activity from Stage 3 is confined to the western edge of Tempe Terra and continues outside the study area to join fault systems around Alba Mons or that track toward the Tharsis Montes. For example, set H11 joins with Tantalus Fossae, a major graben system associated with Alba Mons (Tanaka, 1990). Stage 3 faulting was also active while Tharsis volcanism was ongoing, causing faults to propagate through overlying volcanic flows in some areas; for instance, sets H9 and H10 cut through volcanic units that have buried parts of sets H7 and H8. There is also a variety of small, structurally controlled, plains-style volcanic features that follow local Stage 3 fault trends in the NW of the study area (Moore, 2001; Plescia, 1981). Stage 3 normal faulting is Early to Late Hesperian in both chronology systems, with Hartman-based model ages from 3.5 to 3.3 Ga, and Neukum-based model ages from 3.7 to 3.6 Ga. These results are consistent with the interpretation that Stage 3 activity represents a continuous event with overall NW–SE-oriented extension coinciding with Tharsis volcanic activity that resulted in extensive lava flows. This stage lasted for approximately 130–220 Myr and ended in the Late Hesperian.

Following Stage 3, there appears to have been a major decline in fault activity in Tempe Terra. We have identified only one fault set through the Amazonian and given its small scale and association with glacial features this is likely a reflection of local processes. This indicates that major tectonic activity associated with Tharsis was not occurring in Tempe Terra after the Hesperian. However, it is worth noting that the lack of mapped, Amazonian-age units across the plateau makes clear identification of more recent faulting, including potential reactivation, difficult.

Although we have identified structures ranging in age from Middle Noachian to Amazonian, the majority of tectonic activity in Tempe Terra is extensional in nature and is concentrated in a relatively short period during the Early Hesperian (Figure 9), model ages for which span just 100–170 Myr (Michael, 2013; Werner & Tanaka, 2011). This Early Hesperian activity includes nine fault sets that together comprise 92% of the cumulative fault length in Tempe Terra, as well as the relatively small population of wrinkle ridges. Within the Early Hesperian, tectonic deformation peaked during Stage 2 into early Stage 3, mostly as extensional deformation aligned with the TMAT. This result is in contrast to earlier work, which interpreted a Middle- to Late Noachian peak in faulting at Tempe Terra that then declined through time (Scott & Dohm, 1990). Yet this earlier analysis was based on the unit assignments of Scott and Tanaka (1986), which of course predate the modern availability of high-resolution image data for much of the Martian surface. It is also possible, and even likely given the amount of erosion in the north of Tempe Terra, that we have underestimated the amount of Noachian faulting due to a lack of unit exposure, erosion, and/or later reactivation.

5.3. Oblique Rifting Hypothesis

The prevalence of en echelon graben geometries (Figures 8b and 8c), particularly the system of large en echelon graben associated with the Tempe Rift, indicate that the regional extensional stress fields responsible for the radial faulting in Stages 2 and 3 also had a lateral shear component locally. The scale and pronounced curvature of the en echelon structures that form the central part of the Tempe Rift, which is markedly different to structural features

across the rest of Tempe Terra, suggest a formation mechanism more complex than just simple fault growth through linkage. Fernández and Anguita (2007) proposed sinistral oblique rifting as this mechanism. Oblique rifting consists of both orthogonal pure shear and rift-parallel simple shear (Fernández & Ramírez-Caballero, 2019; Withjack & Jamison, 1986), and is considered the rule rather than the exception for Earth (Brune et al., 2018). Possible sources for oblique tectonics outside of an Earth-like plate tectonic regime are discussed by Fernández and Ramírez-Caballero (2019).

Fernández and Anguita (2007) show that the greatest evidence of obliquity in the Tempe Rift is present at its center, and this transitions to a more orthogonal-dominated rift pattern at either end, particularly to the southwest. Our work is consistent with their hypothesis, although we suggest that evidence of some obliquity continues further to the southwest than the extent of their study, along the full extent of the TMAT exposed at Tempe Terra. Through comparison with previously estimated oblique extension directions along the rift (Fernández & Anguita, 2007; their Figure 14), we find that set H6 is largely orthogonal to the extension direction, while set H5 is typically more oblique to the extension direction but closer to the orientation of the overall rift axis and the alignment of the TMAT (see Figure S2 in Supporting Information S1). We therefore emphasize that the extension directions shown in Figure 9 are a first approximation only and meant as a visual aid for the variation in fault orientations through time. The assumption that extension direction is perpendicular to the average fault orientation breaks down in the case of oblique rifting.

Oblique extension in Tempe Terra is likely controlled by the interplay of several factors, with local-scale (confined to Tempe Terra) heterogeneities interacting with regional-scale (extending over Tharsis) far-field stresses. Structural inheritance and local changes in extension direction around crustal-scale fractures are explanations favored by Fernández and Anguita (2007), and we would add to this the influence of local magmatism. The rift as a whole appears to be controlled by the location of the TMAT, but the areas of highest obliquity likely have the greatest influence of other local factors. We interpret the TMAT as a pre-existing zone of weakness which acted as a locus for extension, controlling the rift axis and main oblique fault trend. This effect is well documented in oblique rifting modeling studies (e.g., Clifton et al., 2000; Duclaux et al., 2020; Tron & Brun, 1991) and, in a similar mechanism, oblique structures in Ulysses Fossae (a region toward the center of Tharsis) have been attributed to a basement transtensional shear zone (Fernández & Ramírez-Caballero, 2019). In addition to this zone of weakness, there is the impact of inherited structures from previous deformation events (Fernández & Anguita, 2007; Hauber & Kronberg, 2001). The prevalence of earlier N-oriented faults from Stage 1 activity could have contributed to the obliquity of the rift if they were reactivated during Stage 2 faulting. The areas of strongest obliquity may therefore provide a guide to the past extent of Stage 1 N-oriented faulting where it has been covered by Hesperian units. An additional factor is the impact of the Labeatis Mons volcanic center, which had its own local stress field as well as likely creating lateral rheological heterogeneity, both of which could affect rift obliquity.

5.4. First Implications for Tharsis Models

If NE-oriented radial normal faulting is considered the hallmark of Tharsis-related extensional deformation in Tempe Terra, then this deformation did not begin in Tempe Terra until the Early Hesperian (or end of the Late Noachian). Our results also place bounds on our estimate of the timing of the TMAT to a discrete period in the beginning of the Early Hesperian, and further provide an interpretation consistent with a relatively late development of the Tharsis Rise.

Of past work that has addressed the relative timing of Tharsis's evolution and its associated tectonic activity, only the model of Bouley et al. (2018) is based on the revised geological map of Tanaka et al. (2014) and is thus directly comparable to ours. Our findings support their major conclusions that extensional and shortening deformation associated with Tharsis as a whole was most active from the Late Noachian to Late Hesperian and peaked in the Early Hesperian (Bouley et al., 2018). However, they cite Tempe Terra as one of two main regions with significant Early to Middle Noachian activity and use faulting in the region's northeast (parts of Mareotis Fossae and the northern Tempe Rift) as some of the earliest evidence of Tharsis growth (Bouley et al., 2018). Here, we have reassigned the ages of these faults from Middle Noachian to Early Hesperian, which further emphasizes the Early Hesperian peak in tectonic activity, but also removes a significant portion of Noachian deformation. This will have knock-on effects to the regional pattern of tectonic activity associated with Tharsis through time and the correlating tectonic centers previously calculated by Anderson et al. (2001).

The deformation history for Tempe Terra we present here also broadly agrees with the model of Tharsis evolution by Tanaka et al. (1991), despite the difference in geological unit ages used. Tanaka et al. (1991) do not address Tharsis activity pre-Late Noachian, but assign structures to two periods of Tharsis-related deformation from the Late Noachian to Amazonian, and these correlate in timing and orientation with our Stage 2 and Stage 3 activity. Our emphasis on Early Hesperian tectonic activity and a slightly later peak in the development of Tharsis is a departure from other studies that propose an early development of Tharsis with a Noachian peak in tectonic activity which then declined (e.g., Anderson et al., 2001; Phillips et al., 2001).

Tempe Terra's large size and location at the edge of the Tharsis Rise, while also having abundant tectonic structures related to Tharsis, makes it well placed to test Tharsis formation models that attempt to reconcile predicted stresses and strain with observed structures. Our results indicate that NW-oriented sets N2, N4, H2 and H3, along with sets H4 and A1, potentially reflect superimposed local activity unrelated to Tharsis and could therefore be excluded from studies of regional tectonic activity. This leaves three significant structural trends of relevance to comparisons with Tharsis formation models: a N trend in Stage 1; a NE trend in Stage 2; and an ENE trend in Stage 3. The NE and ENE trends are broadly consistent with stress patterns predicted by models invoking flexural loading and/or isostasy (e.g., Banerdt et al., 1982; Solomon & Head, 1982; Tanaka et al., 1991; see Banerdt et al. (1992) for maps of these patterns) as well as a plume mechanism (Mège & Masson, 1996). The question of whether the early N-oriented trend is Tharsis-related needs further investigation as it does not match any currently proposed stress model. These shifts in the major deformation orientation between the three stages indicates that no single stress model is likely to fit all the fault data. Oblique extension also complicates assessment of tectonic structures against predicted horizontal stress patterns due to the inherently 3D stress and strain fields it generates (Brune et al., 2018). Existing Tharsis models assume pure extension or compression for Tharsis-related deformation structures, but the presence of a strike-slip component to tectonic activity, even if only active locally, adds more complexity in detail than large-scale models allow, a problem also raised by Fernández and Anguita (2007).

To fully address questions regarding the timing and mechanism of the evolution of Tharsis as a whole, our work on the spatiotemporal evolution of faults in Tempe Terra needs to be linked to more detailed understanding of the sources of faulting and placed into context with the development of other regions on Mars. Logical extensions of this research include characterizing the displacement associated with fault sets in Tempe Terra through time, to more fully characterize the evolution of strain, and the driving stresses, in the region. Comparing displacement–length ratios between sets would offer another way to quantify variations in deformation intensity separate from the cumulative fault length, which has been our primary method here. Measurements of extension and strain for each fault set would also be useful for this purpose and would also provide an opportunity to more robustly establish the sources of stress through time, helping to highlight the active deformation centers during Tharsis's development.

6. Conclusions

Through mapping structures in Tempe Terra in unprecedented detail, we have demonstrated a complex and varied pattern of deformation in this region spanning many hundreds of millions of years early in Martian history. We have been able to capture the full complexity of the structural architecture, refine the region's history of deformation, and provide a catalog of structural features comprising 23,738 normal faults and 142 wrinkle ridges that may be utilized by future researchers. We identified 16 cross-cutting fault sets and placed these in relative order into a timeline of deformation on the basis of a hybrid approach employing cross-cutting relationships and BCC.

Tempe Terra has experienced a multi-phase deformation history with three distinct stages of tectonic activity from the Middle Noachian to the Late Hesperian. Stage 1 produced local zones of N- and NW-striking extensional faulting through the center and west of Tempe Terra from the Middle Noachian to the beginning of the Early Hesperian. Stage 2 produced intense, regional-scale NE faulting concentrated along the Tharsis Montes axial trend in the Early Hesperian and ended with the development of wrinkle ridges in the south of the plateau. Stage 3 generated a pervasive regional network of distributed, ENE-trending graben across most of Tempe Terra from the Early to Late Hesperian. We observe an overall peak in tectonic activity in the Early Hesperian, largely represented by the development of structures along the Tharsis Montes axial trend, and find that Tharsis-related extensional deformation in the form of NE-oriented radial faulting did not begin in Tempe Terra until the Early Hesperian.

Conflict of Interest

The authors declare no conflicts of interest relevant to this study.

Data Availability Statement

The catalog of mapped structural features produced as part of this work is available for download in shapefile format from Zenodo (Orlov, 2022). The crater database created by Lagain et al. (2021) which we used in our buffered crater counting is available to download from Zenodo (Marmo & Lagain, 2020). HRSC and CTX images can be downloaded from NASA's PDS Geoscience Node: HRSC (European Space Agency, 2022 and https://pds-geosciences.wustl.edu/missions/mars_express/hrsc.htm), CTX (Malin, 2007 and https://pds-imaging.jpl.nasa.gov/portal/mro_mission.html). The THEMIS daytime global mosaic (Edwards et al., 2011) and MOLA-HRSC global DEM (Version 2) (Fergason et al., 2018) can be downloaded from the USGS Astropedia Catalog: THEMIS (https://astrogeology.usgs.gov/search/map/Mars/Odyssey/THEMIS-IR-Mosaic-ASU/Mars_MO_THEMIS-IR-Day_mosaic_global_100m_v12), MOLA-HRSC DEM (http://bit.ly/HRSC_MOLA_Blend_v0). Specialist software used in this project is available to download from Github. FracPaQ is available from https://github.com/DaveHealy-github/FracPaQ with description of the software provided in Healy et al. (2017). CSFD Tools is available from https://github.com/ch-riedel/CSFD_Tools with a description of the software provided in Riedel et al. (2018). Craterstats 2.0 is available from https://github.com/ggmichael/craterstats.

Acknowledgments
This work was supported by the University of Leeds International Doctoral Scholarship. We are grateful to NASA and ESA for making Mars data freely available through NASA's Planetary Data System (PDS). We thank Carlos Fernández and an anonymous reviewer for their valuable reviews that improved this paper.

References

Anderson, R. C., Dohm, J. M., Golombek, M. P., Haldemann, A. F. C., Franklin, B. J., Tanaka, K. L., et al. (2001). Primary centers and secondary concentrations of tectonic activity through time in the western hemisphere of Mars. *Journal of Geophysical Research*, *106*(E9), 20563–20585. https://doi.org/10.1029/2000JE001278

Banerdt, W. B., Golombek, M. P., & Tanaka, K. L. (1992). Stress and tectonics on Mars. In H. H. Kieffer, B. M. Jakosky, C. W. Snyder, & M. S. Matthews (Eds.), *Mars* (pp. 249–297). University of Arizona Press.

Banerdt, W. B., Phillips, R. J., Sleep, N. H., & Saunders, R. S. (1982). Thick shell tectonics on one-plate planets: Applications to Mars. *Journal of Geophysical Research*, *87*(B12), 9723–9733. https://doi.org/10.1029/JB087iB12p09723

Barnett, J. A. M., Mortimer, J., Rippon, J. H., Walsh, J. J., & Watterson, J. (1987). Displacement geometry in the volume containing a single normal fault. *AAPG Bulletin*, *71*(8), 925–937. https://doi.org/10.1306/948878ED-1704-11D7-8645000102C1865D

Bouley, S., Baratoux, D., Paulien, N., Missenard, Y., & Saint-Bézar, B. (2018). The revised tectonic history of Tharsis. *Earth and Planetary Science Letters*, *488*, 126–133. https://doi.org/10.1016/j.epsl.2018.02.019

Brune, S., Williams, S. E., & Müller, R. D. (2018). Oblique rifting: The rule, not the exception. *Solid Earth*, *9*(5), 1187–1206. https://doi.org/10.5194/se-9-1187-2018

Butcher, F. E. G., Balme, M. R., Gallagher, C., Arnold, N. S., Conway, S. J., Hagermann, A., & Lewis, S. R. (2017). Recent basal melting of a mid-latitude glacier on Mars. *Journal of Geophysical Research: Planets*, *122*(12), 2445–2468. https://doi.org/10.1002/2017JE005434

Carr, M. H. (1974). Tectonism and volcanism of the Tharsis region of Mars. *Journal of Geophysical Research*, *79*(26), 3943–3949. https://doi.org/10.1029/JB079i026p03943

Christensen, P. R., Jakosky, B. M., Kieffer, H. H., Malin, M. C., McSween, H. Y., Nealson, K., et al. (2004). The thermal emission imaging system (THEMIS) for the Mars 2001 Odyssey mission. *Space Science Reviews*, *110*(1), 85–130. https://doi.org/10.1023/B:SPAC.0000021008.16305.94

Clifton, A. E., Schlische, R. W., Withjack, M. O., & Ackermann, R. V. (2000). Influence of rift obliquity on fault-population systematics: Results of experimental clay models. *Journal of Structural Geology*, *22*(10), 1491–1509. https://doi.org/10.1016/S0191-8141(00)00043-2

Dershowitz, W. S., & Herda, H. H. (1992). Interpretation of fracture spacing and intensity. In *Paper presented at the 33rd U.S. symposium on rock mechanics (USRMS), Santa Fe, New Mexico*.

Duclaux, G., Huismans, R. S., & May, D. A. (2020). Rotation, narrowing, and preferential reactivation of brittle structures during oblique rifting. *Earth and Planetary Science Letters*, *531*, 115952. https://doi.org/10.1016/j.epsl.2019.115952

Edwards, C. S., Nowicki, K. J., Christensen, P. R., Hill, J., Gorelick, N., & Murray, K. (2011). Mosaicking of global planetary image datasets: 1. Techniques and data processing for Thermal Emission Imaging System (THEMIS) multi-spectral data. *Journal of Geophysical Research*, *116*(E10), E10008. https://doi.org/10.1029/2010JE003755

European Space Agency. (2022). MEX-M-HRSC-3-RDR, V4.0 [Dataset]. https://doi.org/10.5270/esa-cjotplq

Fassett, C. I. (2016). Analysis of impact crater populations and the geochronology of planetary surfaces in the inner Solar System. *Journal of Geophysical Research: Planets*, *121*(10), 1900–1926. https://doi.org/10.1002/2016JE005094

Fassett, C. I., & Head, J. W. (2008). The timing of Martian valley network activity: Constraints from buffered crater counting. *Icarus*, *195*(1), 61–89. https://doi.org/10.1016/j.icarus.2007.12.009

Fergason, R. L., Hare, T. M., & Laura, J. (2018). *HRSC and MOLA blended digital elevation model at 200 m v2*. Astrogeology PDS Annex, U.S. Geological Survey. Retrieved from http://bit.ly/HRSC_MOLA_Blend_v0

Fernández, C., & Anguita, F. (2007). Oblique rifting at Tempe Fossae, Mars. *Journal of Geophysical Research*, *112*(E9), E09007. https://doi.org/10.1029/2007JE002889

Fernández, C., & Ramírez-Caballero, I. (2019). Evaluating transtension on Mars: The case of Ulysses Fossae, Tharsis. *Journal of Structural Geology*, *125*, 325–333. https://doi.org/10.1016/j.jsg.2018.05.009

Golombek, M. P., Tanaka, K. L., & Franklin, B. J. (1996). Extension across Tempe Terra, Mars, from measurements of fault scarp widths and deformed craters. *Journal of Geophysical Research*, *101*(E11), 26119–26130. https://doi.org/10.1029/96JE02709

Hartmann, W. K. (2005). Martian cratering 8: Isochron refinement and the chronology of Mars. *Icarus*, *174*(2), 294–320. https://doi.org/10.1016/j.icarus.2004.11.023

Hartmann, W. K., & Neukum, G. (2001). Cratering chronology and the evolution of Mars. *Space Science Reviews*, *96*, 165–194. https://doi.org/10.1007/978-94-017-1035-0_6

Hauber, E., Grott, M., & Kronberg, P. (2010). Martian rifts: Structural geology and geophysics. *Earth and Planetary Science Letters*, *294*(3–4), 393–410. https://doi.org/10.1016/j.epsl.2009.11.005

Hauber, E., & Kronberg, P. (2001). Tempe Fossae, Mars: A planetary analogon to a terrestrial continental rift? *Journal of Geophysical Research*, *106*(E9), 20587–20602. https://doi.org/10.1029/2000JE001346

Healy, D., Rizzo, R. E., Cornwell, D. G., Farrell, N. J. C., Watkins, H., Timms, N. E., et al. (2017). FracPaQ: A MATLAB™ toolbox for the quantification of fracture patterns. *Journal of Structural Geology*, *95*, 1–16. https://doi.org/10.1016/j.jsg.2016.12.003

Henza, A. A., Withjack, M. O., & Schlische, R. W. (2011). How do the properties of a pre-existing normal-fault population influence fault development during a subsequent phase of extension? *Journal of Structural Geology*, *33*(9), 1312–1324. https://doi.org/10.1016/j.jsg.2011.06.010

Ivanov, B. A. (2001). Mars/Moon cratering rate ratio estimates. *Space Science Reviews*, *96*(1), 87–104. https://doi.org/10.1023/A:1011941121102

Jaumann, R., Neukum, G., Behnke, T., Duxbury, T. C., Eichentopf, K., Flohrer, J., et al. (2007). The high-resolution stereo camera (HRSC) experiment on Mars Express: Instrument aspects and experiment conduct from interplanetary cruise through the nominal mission. *Planetary and Space Science*, *55*(7), 928–952. https://doi.org/10.1016/j.pss.2006.12.003

Jenness, J. (2011). *Tools for graphics and shapes: Extension for ArcGIS (version 2.1.85)*. Jenness Enterprises. Retrieved from http://www.jennessent.com/arcgis/shapes_graphics.htm

Kneissl, T., Michael, G. G., Platz, T., & Walter, S. H. G. (2015). Age determination of linear surface features using the Buffered Crater Counting approach—Case studies of the Sirenum and Fortuna Fossae graben systems on Mars. *Icarus*, *250*, 384–394. https://doi.org/10.1016/j.icarus.2014.12.008

Lagain, A., Bouley, S., Baratoux, D., Marmo, C., Costard, F., Delaa, O., et al. (2021). Mars Crater Database: A participative project for the classification of the morphological characteristics of large Martian craters. In W. U. Reimold & C. Koeberl (Eds.), *Large meteorite impacts and planetary evolution VI* (Vol. 550, pp. 629–644). Geological Society of America. https://doi.org/10.1130/2021.2550(29)

Malin, M. C. (2007). MRO context camera experiment data record level 0 V1.0 [Dataset]. NASA Planetary Data System. https://doi.org/10.17189/1520266

Malin, M. C., Bell, J. F., III, Cantor, B. A., Caplinger, M. A., Calvin, W. M., Clancy, R. T., et al. (2007). Context camera investigation on board the Mars Reconnaissance Orbiter. *Journal of Geophysical Research*, *112*(E5), E05S04. https://doi.org/10.1029/2006JE002808

Marmo, C., & Lagain, A. (2020). Alagain/martian_crater_database: Submitted to GSA LMI VI with coherent file renaming (2.2) [Dataset]. Zenodo. https://doi.org/10.5281/zenodo.3633594

McClay, K. R., Dooley, T., Whitehouse, P., & Mills, M. (2002). 4-D Evolution of rift systems: Insights from scaled physical models. *AAPG Bulletin*, *86*(6), 935–959. https://doi.org/10.1306/61EEDBF2-173E-11D7-8645000102C1865D

Mège, D., Cook, A. C., Garel, E., Lagabrielle, Y., & Cormier, M.-H. (2003). Volcanic rifting at Martian grabens. *Journal of Geophysical Research*, *108*(E5), 5044. https://doi.org/10.1029/2002JE001852

Mège, D., & Masson, P. (1996). A plume tectonics model for the Tharsis province, Mars. *Planetary and Space Science*, *44*(12), 1499–1546. https://doi.org/10.1016/S0032-0633(96)00113-4

Michael, G. G. (2013). Planetary surface dating from crater size–frequency distribution measurements: Multiple resurfacing episodes and differential isochron fitting. *Icarus*, *226*(1), 885–890. https://doi.org/10.1016/j.icarus.2013.07.004

Michael, G. G., Kneissl, T., & Neesemann, A. (2016). Planetary surface dating from crater size-frequency distribution measurements: Poisson timing analysis. *Icarus*, *277*, 279–285. https://doi.org/10.1016/j.icarus.2016.05.019

Michael, G. G., & Neukum, G. (2010). Planetary surface dating from crater size–frequency distribution measurements: Partial resurfacing events and statistical age uncertainty. *Earth and Planetary Science Letters*, *294*(3), 223–229. https://doi.org/10.1016/j.epsl.2009.12.041

Moore, J. H. (2001). Geologic map of the Tempe-Mareotis region of Mars (USGS Geologic Investigations Series I-2727). https://doi.org/10.3133/i2727

Nemec, W. (1988). The shape of the rose. *Sedimentary Geology*, *59*(1), 149–152. https://doi.org/10.1016/0037-0738(88)90105-4

Neukum, G., Basilevsky, A. T., Kneissl, T., Chapman, M. G., van Gasselt, S., Michael, G., et al. (2010). The geologic evolution of Mars: Episodicity of resurfacing events and ages from cratering analysis of image data and correlation with radiometric ages of Martian meteorites. *Earth and Planetary Science Letters*, *294*(3), 204–222. https://doi.org/10.1016/j.epsl.2009.09.006

Neukum, G., & Jaumann, R., & HRSC Co-Investigator and Experiment Team. (2004). HRSC: The high resolution stereo camera of Mars express. In A. Wilson (Ed.), *Mars express: The Scientific Payload* (Vol. SP-1240, pp. 17–36). European Space Agency. Retrieved from https://sci.esa.int/s/WEyq9YW

Orlov, C. J. (2022). Tempe Terra fault catalogue (version 1) [Dataset]. Zenodo. https://doi.org/10.5281/zenodo.6531499

Phillips, R. J., Zuber, M. T., Solomon, S. C., Golombek, M. P., Jakosky, B. M., Banerdt, W. B., et al. (2001). Ancient geodynamics and global-scale hydrology on Mars. *Science*, *291*(5513), 2587–2591. https://doi.org/10.1126/science.1058701

Plescia, J. B. (1981). The Tempe volcanic province of Mars and comparisons with the Snake River plains of Idaho. *Icarus*, *45*(3), 586–601. https://doi.org/10.1016/0019-1035(81)90024-5

Plescia, J. B., & Saunders, R. S. (1982). Tectonic history of the Tharsis region, Mars. *Journal of Geophysical Research*, *87*(B12), 9775–9791. https://doi.org/10.1029/JB087iB12p09775

Riedel, C., Michael, G., Kneissl, T., Orgel, C., Hiesinger, H., & van der Bogert, C. H. (2018). A new tool to account for crater obliteration effects in crater size-frequency distribution measurements. *Earth and Space Science*, *5*(6), 258–267. https://doi.org/10.1002/2018EA000383

Schlische, R. W., Withjack, M. O., & Eisenstadt, G. (2002). An experimental study of the secondary deformation produced by oblique-slip normal faulting. *AAPG Bulletin*, *86*(5), 885–906. https://doi.org/10.1306/61EEDBCA-173E-11D7-8645000102C1865D

Scott, D. H., & Dohm, J. M. (1990). Faults and ridges: Historical development in Tempe Terra and Ulysses Patera regions of Mars. In *Proceedings of the 20th lunar and planetary science conference* (pp. 503–513). Retrieved from https://ui.adsabs.harvard.edu/abs/1990LPSC…20…503S

Scott, D. H., & Tanaka, K. L. (1986). Geologic map of the western equatorial region of Mars (USGS Miscellaneous Investigations Series Map I-1802-A). https://doi.org/10.3133/i1802A

Solomon, S. C., & Head, J. W. (1982). Evolution of the Tharsis Province of Mars: The importance of heterogeneous lithospheric thickness and volcanic construction. *Journal of Geophysical Research*, *87*(B12), 9755–9774. https://doi.org/10.1029/JB087iB12p09755

Tanaka, K. L. (1982). *A new time-saving crater-count technique, with application to narrow features. Reports of Planetary Geology Program(TM-85127)* (pp. 123–125). NASA Technical Memo. Retrieved from https://ui.adsabs.harvard.edu/abs/1982pggp.rept.123T

Tanaka, K. L. (1990). Tectonic history of the Alba Patera-Ceraunius Fossae region of Mars. In *Proceedings of the 20th lunar and planetary science conference* (pp. 515–523). Retrieved from https://ui.adsabs.harvard.edu/abs/1990LPSC…20…515T

Tanaka, K. L., Golombek, M. P., & Banerdt, W. B. (1991). Reconciliation of stress and structural histories of the Tharsis region of Mars. *Journal of Geophysical Research*, *96*(E1), 15617–15633. https://doi.org/10.1029/91JE01194

Tanaka, K. L., Skinner, J. A., Dohm, J. M., Irwin, R. P., III, Kolb, E. J., Fortezzo, C. M., et al. (2014). Geologic map of Mars. (USGS Scientific Investigations Map 3292). https://doi.org/10.3133/sim3292

Tron, V., & Brun, J.-P. (1991). Experiments on oblique rifting in brittle-ductile systems. *Tectonophysics*, *188*(1), 71–84. https://doi.org/10.1016/0040-1951(91)90315-J

Watters, T. R., & Maxwell, T. A. (1983). Crosscutting relations and relative ages of ridges and faults in the Tharsis region of Mars. *Icarus*, *56*(2), 278–298. https://doi.org/10.1016/0019-1035(83)90039-8

Werner, S. C., & Tanaka, K. L. (2011). Redefinition of the crater-density and absolute-age boundaries for the chronostratigraphic system of Mars. *Icarus*, *215*(2), 603–607. https://doi.org/10.1016/j.icarus.2011.07.024

Wilkins, S. J., & Schultz, R. A. (2001). Structural style and mode of extension in the northern Tempe Rift. In *Paper presented at the lunar and planetary science conference XXXII, Houston, Texas*.

Wilkins, S. J., Schultz, R. A., Anderson, R. C., Dohm, J. M., & Dawers, N. H. (2002). Deformation rates from faulting at the Tempe Terra extensional province, Mars. *Geophysical Research Letters*, *29*(18), 31-1–31-4. https://doi.org/10.1029/2002GL015391

Wilson, L., & Head, J. W. (2002). Tharsis-radial graben systems as the surface manifestation of plume-related dike intrusion complexes: Models and implications. *Journal of Geophysical Research*, *107*(E8), 5057. https://doi.org/10.1029/2001JE001593

Wise, D. U., Golombek, M. P., & McGill, G. E. (1979). Tharsis province of Mars: Geologic sequence, geometry, and a deformation mechanism. *Icarus*, *38*(3), 456–472. https://doi.org/10.1016/0019-1035(79)90200-8

Withjack, M. O., & Jamison, W. R. (1986). Deformation produced by oblique rifting. *Tectonophysics*, *126*(2), 99–124. https://doi.org/10.1016/0040-1951(86)90222-2

Wyrick, D., Ferrill, D. A., Morris, A. P., Colton, S. L., & Sims, D. (2004). Distribution, morphology, and origins of Martian pit crater chains. *Journal of Geophysical Research*, *109*(E6), E06005. https://doi.org/10.1029/2004JE002240

Zhong, S. (2009). Migration of Tharsis volcanism on Mars caused by differential rotation of the lithosphere. *Nature Geoscience*, *2*(1), 19–23. https://doi.org/10.1038/ngeo392